nature portfolio

https://doi.org/10.1038/s41586-025-08899-y

Supplementary information

Quantum error correction of qudits beyond break-even

In the format provided by the authors and unedited

Supplementary Information
"Quantum Error Correction of Qudits Beyond Break-even"

Benjamin L. Brock,* Shraddha Singh, Alec Eickbusch,† Volodymyr V. Sivak,†
Andy Z. Ding, Luigi Frunzio, Steven M. Girvin, and Michel H. Devoret‡

Departments of Applied Physics and Physics, Yale University, New Haven, CT, USA
Yale Quantum Institute, Yale University, New Haven, CT, USA

(Dated: April 24, 2025)

CONTENTS

* benjamin.brock@yale.edu
† Present address: Google Quantum AI, Santa Barbara, CA
‡ michel.devoret@yale.edu; Present addresses: UC Santa Barbara Dept. of Physics and Google Quantum AI, Santa Barbara, CA

I. EXPERIMENTAL DEVICE AND METHODS

In this work we use the same experimental device as in [1]. It consists of a tantalum transmon fabricated on a sapphire chip [2–4], which is inserted into a waveguide tunnel connected to a high-Q $\lambda/4$ 3D microwave cavity machined out of high purity aluminum [5, 6]. We use the fundamental mode of the cavity as our oscillator (described by operator a, with Fock states $\{|0\rangle, |1\rangle, ...\}$), and the transmon's ground $|g\rangle$ and excited $|e\rangle$ states as our ancilla qubit (described by Pauli operators $\sigma_{x,y,z}$). The dipole coupling between the transmon and cavity gives rise to a dispersive coupling between these modes. Co-fabricated on the sapphire chip are a stripline readout resonator and Purcell filter, for dispersively measuring the state of the transmon qubit. We characterize the device and calibrate our control pulses using the methods described in detail in Ref. [1]. For the sake of brevity, in this section we limit ourselves to describing our experimental methods when they either differ from those used previously, or are important for contextualizing our results.

We model the idling Hamiltonian of the transmon-cavity system, in the rotating frame of both the cavity (frequency ω_c) and transmon qubit (frequency ω_q), as

$$H_0/\hbar = \frac{1}{2}\chi a^\dagger a \sigma_z + \frac{1}{2}K a^{\dagger 2} a^2 + \frac{1}{4}\chi' a^{\dagger 2} a^2 \sigma_z, \tag{S1}$$

where χ is the dispersive shift, χ' is the second-order dispersive shift, and K is the Kerr nonlinearity. In Table S I we present values for these parameters, measured in the same time-frame as the rest of our reported results. Our measurements of the transmon and cavity lifetimes are presented in Fig. S 1. Due to the presence of a two-level system (TLS) coupled to our transmon we find beats in the Ramsey coherence measurement. Note that our measured value of the cavity pure-dephasing rate is

$$\kappa_{\phi,c} = \frac{1}{T_{2R,c}} - \frac{1}{2T_{1,c}} = (5.6 \pm 0.6 \text{ ms})^{-1}, \tag{S2}$$

which differs from from the rate of dephasing $\kappa_{\phi,c}^{(n_{\text{th}})}$ induced by transmon thermal fluctuations

$$\kappa_{\phi,c}^{(n_{\text{th}})} \approx \frac{n_{\text{nth}}}{T_{1,q}} = (13.4 \pm 0.6 \text{ ms})^{-1}, \tag{S3}$$

where the approximation we used for $\kappa_{\phi,c}^{(n_{\text{th}})}$ is valid in the regime $\chi \gg T_{1,q}^{-1}$ and $n_{\text{th}} \ll 1$ [7, 8]. A similar discrepancy was found in Ref. [1]. Since we expect our 3D cavity to have negligible intrinsic dephasing [5, 9–11], we attribute this discrepancy to systematic error in our $T_{2R,c}$ measurement. In particular, we expect that errors during the echoed conditional displacement (ECD) circuit used in this measurement [1] cause leakage outside the $\{|0\rangle, |1\rangle\}$ subspace of the cavity, leading to an apparent reduction of $T_{2R,c}$.

The stability of our system is well-captured by the measurements reported in [1]. The primary source of fluctuations are spurious two-level-systems coming into and out of resonance with the transmon, causing fluctuations in the transmon lifetimes. These fluctuations typically occur on a week-by-week timescale. Our training and evaluation of the optimal GKP qubit, qutrit, and ququart were performed during periods of stability well-described by the reported experimental parameters.

A. ECD Pulse Compilation

We compile our echoed conditional displacement (ECD) gates [12] in terms of displacements $D(\alpha) = \exp(\alpha a^\dagger - \alpha^* a)$, ancilla rotations, and evolution $U_0(\tau) = e^{-iH_0\tau/\hbar}$ under the idling Hamiltonian of Eq. (S1) for time τ. Our compilation takes the form

$$\text{ECD}(\beta;\alpha,\tau) = D(i\alpha e^{i\theta_\beta}\cos 2\phi)\ U_0(\tau)\ D(-i\alpha e^{i\theta_\beta}\cos\phi)\ \sigma_x\ D(-i\alpha e^{i\theta_\beta}\cos\phi)\ U_0(\tau)\ D(i\alpha e^{i\theta_\beta}), \tag{S4}$$

where $\beta = |\beta|e^{i\theta_\beta}$ is the conditional displacement amplitude, $\alpha \in \mathbb{R}_{\geq 0}$ is the intermediate displacement amplitude, $\phi = \chi(\tau + \tau_{\text{disp}})/2$, $\tau_{\text{disp}} = 48$ ns is the duration of our cavity displacement pulses, and τ is the wait time required to achieve the desired $|\beta|$ given the intermediate amplitude α. Following Ref. [1], we calibrate the wait time $\tau(\alpha, \beta)$ empirically using the model

$$\tau(\alpha, \beta) = p_1 \left|\frac{\beta}{\alpha}\right| - p_2, \tag{S5}$$

Cavity mode	Frequency	$\omega_c = 2\pi \times 4.479$ GHz
	1st order dispersive shift	$\chi = 2\pi \times 41.8$ kHz
	2nd order dispersive shift	$\chi' = 2\pi \times 4.3$ Hz
	Kerr nonlinearity	$K = -2\pi \times 3.7$ Hz
	Energy Relaxation	$T_{1,c} = 631 \pm 3$ μs
	Dephasing (Ramsey)	$T_{2R,c} = 1030 \pm 20$ μs
Ancilla transmon	Frequency	$\omega_q = 2\pi \times 6.009$ GHz
	Anharmonicity	$\alpha_q = -2\pi \times 221$ MHz
	Thermal Population	$n_{\mathrm{th}} = 2.2 \pm 0.1\%$
	Energy Relaxation	$T_{1,q} = 295 \pm 1$ μs
	Dephasing (Ramsey)	$T_{2R,q} = 181 \pm 5$ μs
	Dephasing (Echo)	$T_{2E,q} = 286 \pm 1$ μs
Readout resonator	Frequency	$\omega_r = 2\pi \times 9.110$ GHz
	Dispersive shift	$\chi_{qr} = 2\pi \times 0.60$ MHz
	Coupling strength	$\kappa_{r,\mathrm{ext}} = 2\pi \times 0.47$ MHz
	Internal loss	$\kappa_{r,\mathrm{int}} = 2\pi \times 0.03$ MHz

Table S I. Measured system parameters.

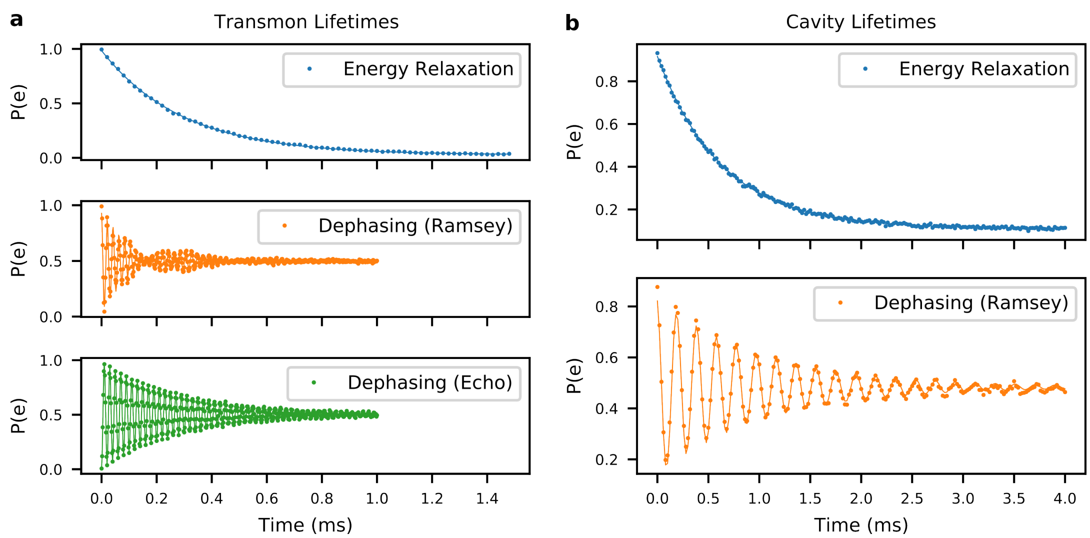

FIG. S 1. **a**, Transmon and **b**, Cavity lifetimes. The fit values are presented in Table S I.

and find typical values of $p_1 \approx 1566$ ns and $p_2 \approx 48$ ns. We also calibrate the geometric phase accumulated by the ancilla qubit during each ECD gate following established methods [1, 12]. Compiling our ECD gates in terms of these primitive pulses, rather than long array pulses, gives us the flexibility to realize the complicated control sequences required for manipulating GKP qudits.

B. Oscillator State Preparation

We prepare arbitrary oscillator states using ECD gates $\mathrm{ECD}(\beta) = D(\beta/2)|e\rangle\langle g| + D(-\beta/2)|g\rangle\langle e|$ and ancilla qubit rotations $R_\phi(\theta) = \exp[i(\sigma_x \cos\phi + \sigma_y \sin\phi)\theta/2]$, which together enable universal control of the combined qubit-oscillator system [12]. In particular, we can approximate the unitary operator U_ψ that maps the state $|g\rangle|0\rangle$ to the target state $|g\rangle|\psi\rangle$ with the interleaved sequence

$$U_\psi \approx U_\psi(\vec{\beta}, \vec{\phi}, \vec{\theta}) = \mathrm{ECD}(\beta_N) R_{\phi_N}(\theta_N) \mathrm{ECD}(\beta_{N-1}) R_{\phi_{N-1}}(\theta_{N-1}) \cdots \mathrm{ECD}(\beta_1) R_{\phi_1}(\theta_1), \tag{S6}$$

where we refer to N as the depth of the ECD circuit. We optimize this unitary offline [13], with a fixed circuit depth, finding the circuit parameters $\vec{\beta}$, $\vec{\phi}$, and $\vec{\theta}$ that maximize the fidelity $\mathcal{F} = |\langle g|\langle\psi|U_\psi(\vec{\beta}, \vec{\phi}, \vec{\theta})|g\rangle|0\rangle|^2$ in the absence of loss.

C. Wigner and Characteristic Function Tomography

We measure the state of our oscillator mode by performing either Wigner tomography or characteristic function tomography. The Wigner function can be defined as the expectation value of the displaced photon-number parity operator $\Pi = e^{i\pi a^\dagger a}$ according to

$$W(\alpha) = \langle D(\alpha)\Pi D(-\alpha)\rangle. \tag{S7}$$

We map the photon-number parity to the ancilla qubit by initializing the ancilla in $|+\rangle = (|g\rangle + |e\rangle)/\sqrt{2}$ and evolving under the dispersive Hamiltonian $H_{\rm disp} = \chi a^\dagger a\sigma_z/2$ for time $t = \pi/\chi$, such that

$$|+\rangle \sum_{n=0}^{\infty} c_n|n\rangle \to e^{-i\pi a^\dagger a\sigma_z/2}|+\rangle \sum_{n=0}^{\infty} c_n|n\rangle = |+\rangle \sum_{n\text{ even}}^{\infty} i^n c_n|n\rangle + |-\rangle \sum_{n\text{ odd}}^{\infty} i^n c_n|n\rangle, \tag{S8}$$

where $|-\rangle = (|g\rangle - |e\rangle)/\sqrt{2}$ [14]. Afterwards, we rotate the ancilla around its y axis by applying $R_{\pi/2}(-s\pi/2)$ and measuring σ_z of the ancilla, such that the measurement result $\sigma_z = \pm 1$ corresponds to the parity result $\Pi = \pm s$, where $s = \pm 1$. In practice we symmetrize this measurement by using $s = 1$ half the time and $s = -1$ half the time. To measure $W(\alpha)$, we simply prepend this parity measurement with a cavity displacement $D(-\alpha)$. To reconstruct density matrices from Wigner tomography measurements we follow the method described in Ref. [1].

The characteristic function $\mathcal{C}(\beta)$ is defined as the expectation value of the displacement operator $\langle D(\beta)\rangle$ and it is also the Fourier transform of the Wigner function, which is why we often call β-space reciprocal phase space. Following previous work [12, 15, 16], we map the characteristic function of the cavity state $|\psi\rangle$ to our ancilla qubit by performing an ECD gate starting with our ancilla in the $|+\rangle$ state. This entangles the cavity with the ancilla according to

$$\text{ECD}(\beta)|+\rangle|\psi\rangle = \frac{1}{\sqrt{2}}\Big[|g\rangle D(-\beta/2)|\psi\rangle + |e\rangle D(\beta/2)|\psi\rangle\Big]. \tag{S9}$$

Tracing out the cavity, the reduced density matrix on our qubit can be written

$$\rho_q = \frac{1}{2}\begin{pmatrix} 1 & \langle D(-\beta)\rangle \\ \langle D(\beta)\rangle & 1 \end{pmatrix}, \tag{S10}$$

such that the characteristic function is encoded in expectation values of the qubit with respect to the equator of its Bloch sphere according to

$$\langle D(\beta)\rangle = \langle \sigma_x\rangle + i\langle\sigma_y\rangle. \tag{S11}$$

The derivatives of the characteristic function at the origin of reciprocal phase space enable us to measure photon statistics of the field in the cavity according to [15]

$$\langle a^{\dagger m} a^n\rangle = -\frac{\partial^{m+n}}{\partial\beta^m \partial(\beta^*)^n}\mathcal{C}(\beta)\Big|_{\beta=0}. \tag{S12}$$

In particular, for $\beta = x + iy$ the average number of photons in the cavity can be written

$$\langle a^\dagger a\rangle = -\frac{1}{2} - \frac{1}{4}\left[\frac{\partial^2\mathcal{C}}{\partial x^2} + \frac{\partial^2\mathcal{C}}{\partial y^2}\right]_{\substack{x=0\\y=0}}. \tag{S13}$$

II. GOTTESMAN-KITAEV-PRESKILL QUDITS

In its most general form, the Gottesman-Kitaev-Preskill (GKP) code can be used to encode a logical qudit within N oscillator modes [17]. As discussed in the main text, we restrict ourselves to the single-mode square code with ideal stabilizer generators

$$S_X = D(\ell_d) \;= e^{-i\ell_d\sqrt{2}p}, \tag{S14}$$

$$S_Z = D(i\ell_d) = e^{i\ell_d\sqrt{2}q}, \tag{S15}$$

ideal codewords

$$|Z_n\rangle_d \propto \sum_{k=-\infty}^{\infty} |n\sqrt{2\pi/d} + k\sqrt{2\pi d}\rangle_q \tag{S16}$$

with $n = 0, 1, ..., d-1$, and ideal logical Pauli operators

$$X_d = D(\ell_d/d) \ = e^{-i\ell_d\sqrt{2}p/d}, \tag{S17}$$

$$Z_d = D(i\ell_d/d) = e^{i\ell_d\sqrt{2}q/d}, \tag{S18}$$

where $\ell_d = \sqrt{\pi d}$ and $d \in \mathbb{Z}_{>0}$ is the dimension of the logical qudit. Note that with our choice of phase-space units, translations in position and displacements along the real axis of phase space differ in amplitude by a factor of $\sqrt{2}$. The Pauli operators act on the Z-codewords according to

$$\begin{aligned} Z_d|Z_n\rangle_d &= \omega_d^n|Z_n\rangle_d, \\ X_d|Z_n\rangle_d &= |Z_{(n+1) \bmod d}\rangle_d, \\ Z_d X_d &= \omega_d X_d Z_d, \end{aligned} \tag{S19}$$

where $\omega_d = e^{2\pi i/d}$ is the primitive dth root of unity. Here the oscillator is described by mode operator a, position operator $q = (a + a^\dagger)/\sqrt{2}$, momentum operator $p = i(a^\dagger - a)/\sqrt{2}$, and displacement operator $D(\alpha) = \exp\left(\alpha a^\dagger - \alpha^* a\right)$.

The eigenstates of the generalized Pauli operators play a key role in our experiment. For Pauli operator P_d with non-degenerate spectrum $\{1, \omega_d, \omega_d^2, ..., \omega_d^{d-1}\}$, we define the nth eigenstate $|P_n\rangle_d$ according to

$$P_d|P_n\rangle_d = \omega_d^n|P_n\rangle_d. \tag{S20}$$

To ensure P_d has the desired spectrum we either define it as $X_d^n Z_d^m$ or $\sqrt{\omega_d}X_d^n Z_d^m$, for integers n and m. Note that we sometimes omit subscripts d and/or the factor of $\sqrt{\omega_d}$ for convenience, when the meaning remains contextually clear. We present the Pauli eigenstates of the qubit, qutrit, and ququart used throughout this work in terms of the Pauli Z_d basis states in Table S II. We find these representations by numerically diagonalizing the relevant operators. In this table we also present the ququart parity basis $\{|\pm, n\rangle_4; s = \pm, n = 0, 1\}$, which are the simultaneous eigenstates of X_4^2 and Z_4^2 according to $X_4^2|\pm, n\rangle_4 = \pm|\pm, n\rangle_4$ and $Z_4^2|\pm, n\rangle_4 = (-1)^n|\pm, n\rangle_4$, in terms of the Z_d basis.

In practice, we work with an approximate finite-energy version of the GKP code, obtained by applying the Gaussian envelope operator $E_\Delta = \exp\left(-\Delta^2 a^\dagger a\right)$ to both the operators O and states $|\psi\rangle$ of the ideal code according to[17, 18]

$$\begin{aligned} |\psi\rangle_\Delta &= E_\Delta|\psi\rangle, \\ O_\Delta &= E_\Delta O E_\Delta^{-1}, \end{aligned} \tag{S21}$$

up to normalization. The parameter Δ determines both the squeezing of individual quadrature peaks in the grid states as well as their overall extent in energy.

To find the finite-energy Pauli eigenstates numerically, we extend the approach of Ref. [12] to the case of GKP qudits. We find the finite-energy $|Z_0\rangle_{d,\Delta}$ state by computing the ground state of the fictitious Hamiltonian

$$H = -\frac{1}{2}E_\Delta\left(S_X + S_X^\dagger\right)E_\Delta^{-1} - \frac{1}{2}E_\Delta\left(S_Z + S_Z^\dagger\right)E_\Delta^{-1} - dE_\Delta\left(Z_d + Z_d^\dagger\right)E_\Delta^{-1}, \tag{S22}$$

and then obtain the remaining $|Z_n\rangle_{d,\Delta}$ states according to

$$|Z_n\rangle_{d,\Delta} = E_\Delta X_d^n E_\Delta^{-1}|Z_0\rangle_{d,\Delta}. \tag{S23}$$

Finally, we obtain the remaining states using the expressions in Table S II.

A. Stabilizing Finite-energy GKP Qudits

We follow Ref. [19] to generalize the sBs protocol to stabilize finite-energy GKP qudits. The stabilizers (S) of the ideal square GKP qudit are given by $S_Z = e^{i\sqrt{2\pi d}q}, S_X = e^{-i\sqrt{2\pi d}p}$. The finite-energy analog of these stabilizers can be expressed as

$$S_{Z,\Delta} = e^{i\sqrt{2\pi d}(q\cosh\Delta^2 + ip\sinh\Delta^2)}, \tag{S24}$$

$$S_{X,\Delta} = e^{-i\sqrt{2\pi d}(p\cosh\Delta^2 - iq\sinh\Delta^2)}. \tag{S25}$$

Qubit Pauli States	$n=0$	$n=1$
$\|X_n\rangle_2$	$\|Z_0\rangle_2 + \|Z_1\rangle_2$	$\|Z_0\rangle_2 - \|Z_1\rangle_2$
$\|\sqrt{\omega}XZ_n\rangle_2$	$\|Z_0\rangle_2 + \sqrt{\omega}\|Z_1\rangle_2$	$\|Z_0\rangle_2 - \sqrt{\omega}\|Z_1\rangle_2$

Qutrit Pauli States	$n=0$	$n=1$	$n=2$
$\|X_n\rangle_3$	$\|Z_0\rangle_3 + \|Z_1\rangle_3 + \|Z_2\rangle_3$	$\|Z_0\rangle_3 + \omega^2\|Z_1\rangle_3 + \omega\|Z_2\rangle_3$	$\|Z_0\rangle_3 + \omega\|Z_1\rangle_3 + \omega^2\|Z_2\rangle_3$
$\|XZ_n\rangle_3$	$\|Z_0\rangle_3 + \|Z_1\rangle_3 + \omega\|Z_2\rangle_3$	$\|Z_0\rangle_3 + \omega^2\|Z_1\rangle_3 + \omega^2\|Z_2\rangle_3$	$\|Z_0\rangle_3 + \omega\|Z_1\rangle_3 + \|Z_2\rangle_3$
$\|X^2Z_n\rangle_3$	$\|Z_0\rangle_3 + \omega^2\|Z_1\rangle_3 + \|Z_2\rangle_3$	$\|Z_0\rangle_3 + \|Z_1\rangle_3 + \omega^2\|Z_2\rangle_3$	$\|Z_0\rangle_3 + \omega\|Z_1\rangle_3 + \omega\|Z_2\rangle_3$

Ququart Pauli States	$n=0$	$n=1$	$n=2$	$n=3$
$\|X_n\rangle_4$	$\|Z_0\rangle_4 + \|Z_1\rangle_4$ $+\|Z_2\rangle_4 + \|Z_3\rangle_4$	$\|Z_0\rangle_4 - \omega\|Z_1\rangle_4$ $-\|Z_2\rangle_4 + \omega\|Z_3\rangle_4$	$\|Z_0\rangle_4 - \|Z_1\rangle_4$ $+\|Z_2\rangle_4 - \|Z_3\rangle_4$	$\|Z_0\rangle_4 + \omega\|Z_1\rangle_4$ $-\|Z_2\rangle_4 - \omega\|Z_3\rangle_4$
$\|\sqrt{\omega}XZ_n\rangle_4$	$\|Z_0\rangle_4 + \sqrt{\omega}\|Z_1\rangle_4$ $-\|Z_2\rangle_4 + \sqrt{\omega}\|Z_3\rangle_4$	$\sqrt{\omega}\|Z_0\rangle_4 + \|Z_1\rangle_4$ $+\sqrt{\omega}\|Z_2\rangle_4 - \|Z_3\rangle_4$	$\|Z_0\rangle_4 - \sqrt{\omega}\|Z_1\rangle_4$ $-\|Z_2\rangle_4 - \sqrt{\omega}\|Z_3\rangle_4$	$\sqrt{\omega}\|Z_0\rangle_4 - \|Z_1\rangle_4$ $+\sqrt{\omega}\|Z_2\rangle_4 + \|Z_3\rangle_4$
$\|X^2Z_n\rangle_4$	$\|Z_1\rangle_4 + \omega\|Z_3\rangle_4$	$\|Z_0\rangle_4 - \omega\|Z_2\rangle_4$	$\|Z_1\rangle_4 - \omega\|Z_3\rangle_4$	$\|Z_0\rangle_4 + \omega\|Z_2\rangle_4$
$\|\sqrt{\omega}X^3Z_n\rangle_4$	$\|Z_0\rangle_4 - \sqrt{\omega}\|Z_1\rangle_4$ $+\|Z_2\rangle_4 + \sqrt{\omega}\|Z_3\rangle_4$	$\sqrt{\omega}\|Z_0\rangle_4 + \|Z_1\rangle_4$ $-\sqrt{\omega}\|Z_2\rangle_4 + \|Z_3\rangle_4$	$\|Z_0\rangle_4 + \sqrt{\omega}\|Z_1\rangle_4$ $+\|Z_2\rangle_4 - \sqrt{\omega}\|Z_3\rangle_4$	$\sqrt{\omega}\|Z_0\rangle_4 - \|Z_1\rangle_4$ $-\sqrt{\omega}\|Z_2\rangle_4 - \|Z_3\rangle_4$
$\|XZ_n^2\rangle_4$	$\|Z_0\rangle_4 + \|Z_1\rangle_4$ $-\|Z_2\rangle_4 - \|Z_3\rangle_4$	$\|Z_0\rangle_4 - \omega\|Z_1\rangle_4$ $+\|Z_2\rangle_4 - \omega\|Z_3\rangle_4$	$\|Z_0\rangle_4 - \|Z_1\rangle_4$ $-\|Z_2\rangle_4 + \|Z_3\rangle_4$	$\|Z_0\rangle_4 + \omega\|Z_1\rangle_4$ $+\|Z_2\rangle_4 + \omega\|Z_3\rangle_4$

Ququart Parity States	$\|+,0\rangle_4$	$\|-,0\rangle_4$	$\|+,1\rangle_4$	$\|-,1\rangle_4$
	$\|Z_0\rangle_4 + \|Z_2\rangle_4$	$\|Z_0\rangle_4 - \|Z_2\rangle_4$	$\|Z_1\rangle_4 + \|Z_3\rangle_4$	$\|Z_1\rangle_4 - \|Z_3\rangle_4$

Table S II. Pauli eigenstates of the qubit, qutrit, and ququart expressed in the Z_d basis, and the ququart parity states expressed in the Z_4 basis. For each qudit, $\omega = e^{2\pi i/d}$ is the primitive dth root of unity and $\sqrt{\omega} = e^{i\pi/d}$. The overall normalization constants are omitted for simplicity.

To construct the engineered dissipation onto the codespace of these finite-energy stabilizers, we introduce an effective mode operator $a_{X,Z} \propto \log(S_{X,Z})$ which annihilates the GKP qudit codewords. These mode operators can be written

$$a_Z = (q_{[\sqrt{2\pi/d}]} + ip\tanh\Delta^2)/\sqrt{2\tanh\Delta^2}, \tag{S26}$$

$$a_X = (p_{[\sqrt{2\pi/d}]} - iq\tanh\Delta^2)/\sqrt{2\tanh\Delta^2}. \tag{S27}$$

Here $v_{[m]}$ denotes the symmetric version of the modular quadrature $v \pmod m$, also known as the Zak-basis [20].

To realize our engineered dissipation, we siphon energy from the operator $a_{X,Z}$ into an ancilla qubit by evolving under

$$H \propto a_{X,Z}(\sigma_x - i\sigma_y) + a^\dagger_{X,Z}(\sigma_x + i\sigma_y) \tag{S28}$$

for a short time, resetting the ancilla, and repeating. Resetting the ancilla extracts entropy from the oscillator in a way that stabilizes the ground state manifold of $a_{X,Z}$, which is designed to be the finite-energy GKP qudit codespace. Starting with the ancilla in $|g\rangle$, the desired entangling unitary associated with a_Z can be expressed

$$U_Z = \exp\left[-i\sqrt{\frac{\gamma\delta t}{\tanh\Delta^2}}\left(q_{[\sqrt{2\pi/d}]}\sigma_x + p\sigma_y\tanh\Delta^2\right)\right], \tag{S29}$$

where γ is the rate of dissipation onto the ground state of a_Z. We can now use second-order trotterization of U_Z to derive the circuit that stabilizes the logical Z subspace,

$$U_Z^{\mathrm{sBs}} = \exp\left(-i\sqrt{\frac{\gamma\delta t\tanh(\Delta^2)}{4}}p\sigma_y\right)\exp\left(-i\sqrt{\frac{\gamma\delta t}{\tanh(\Delta^2)}}q_{[\sqrt{2\pi/d}]}\sigma_x\right)\exp\left(-i\sqrt{\frac{\gamma\delta t\tanh(\Delta^2)}{4}}p\sigma_y\right) + \mathcal{O}[(\gamma\delta t)^{3/2}]. \tag{S30}$$

Since the modular quadratures are translation invariant we impose the constraint $q_{[\sqrt{2\pi/d}]} \to q$ on the trotterized unitary, and choose

$$\gamma\delta t = \frac{\pi d}{2}\tanh\Delta^2\left(\cosh\Delta^2\right)^2. \tag{S31}$$

Plugging back in, we obtain

$$U_Z^{\mathrm{sBs}} = \exp\left(-i\varepsilon_d p\sigma_y/2\sqrt{2}\right)\exp\left(-i\ell_{d,\Delta}q\sigma_x/\sqrt{2}\right)\exp\left(-i\varepsilon_d p\sigma_y/2\sqrt{2}\right), \tag{S32}$$

where $\varepsilon_d = \sqrt{\pi d}\sinh\Delta^2$ and $\ell_{d,\Delta} = \sqrt{\pi d}\cosh\Delta^2$. We next introduce Hadamard gates H and ancilla rotations to express the circuit in terms of conditional displacement gates conditioned on the σ_z axis of the ancilla Bloch sphere, as used in the main text. Doing so, we obtain

$$U_Z^{\mathrm{sBs}} = \exp\left(-i\varepsilon_d p\sigma_z/2\sqrt{2}\right)R_0^\dagger(\pi/2)\exp\left(-i\ell_{d,\Delta}q\sigma_z/\sqrt{2}\right)R_0(\pi/2)\exp\left(-i\varepsilon_d p\sigma_z/2\sqrt{2}\right), \tag{S33}$$

where we now assume that we begin with the ancilla in $|+\rangle$ rather than $|g\rangle$ (and we ignore ancilla gates at the end since we follow the last entangling operation with a reset). This circuit can be expressed in terms of ECD gates as

$$U_Z^{\mathrm{sBs}} = \mathrm{ECD}(\varepsilon_d/2)\ R_0(\pi/2)\ \mathrm{ECD}(-i\ell_{d,\Delta})\ R_0^\dagger(\pi/2)\ \mathrm{ECD}(\varepsilon_d/2). \tag{S34}$$

If we update the cavity reference phase by a factor of i, we obtain the circuit in Fig. 1c of the main text.

B. Maximally-mixed GKP Qudit States

Since the codespace of the GKP qudit is the steady state of the engineered dissipation realized by the sBs protocol, we can prepare the maximally mixed state ρ_d^{mix} by turning on sBs and waiting, as discussed in the main text. In Fig. S 2a we reproduce the dataset presented in Fig. 1d of the main text, but here we include our measurement of $\mathrm{Im}[\mathcal{C}]$ as well, which is zero as we expect. In Fig. S 2b we plot the simulated Wigner functions of these mixed states.

Interestingly, the maximally mixed GKP states in odd dimension d have regions of Wigner negativity, indicating non-classicality [21]. This can be viewed as a consequence of the interference fringes of the $|Z_n\rangle_d$ basis states in phase

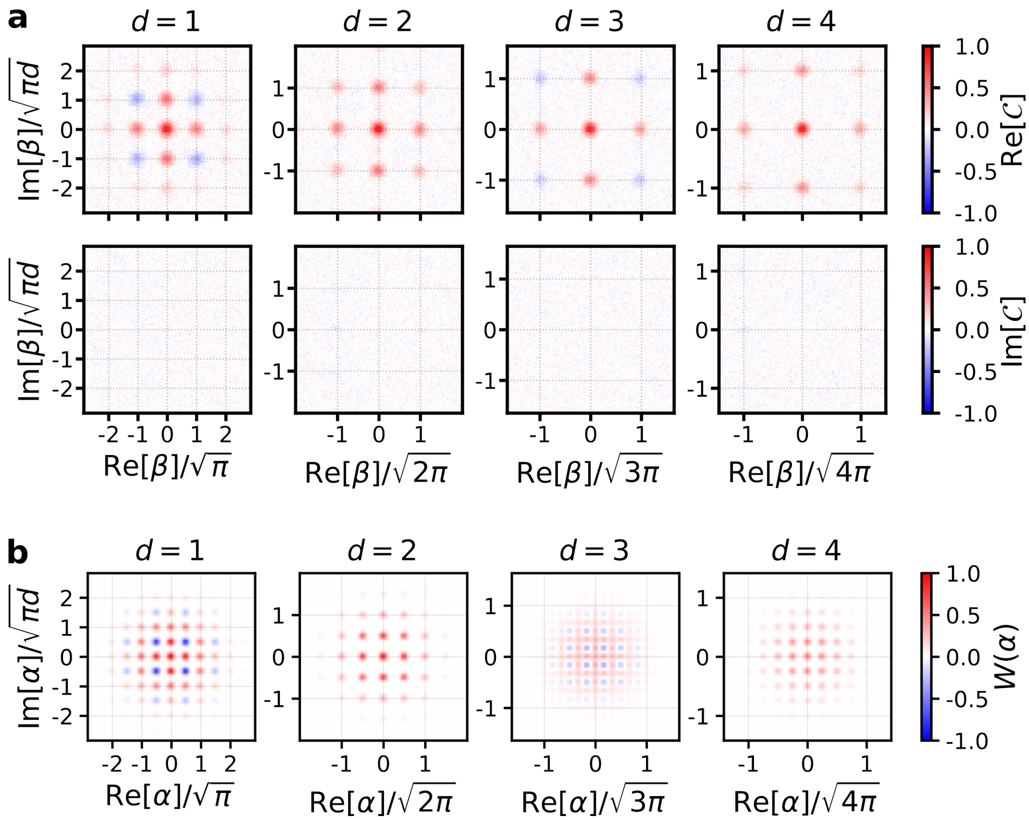

FIG. S 2. **Maximally-mixed GKP qudit states.** **a**, Measured characteristic functions of the maximally-mixed states of GKP qudits. This is the same dataset presented in Fig. 1d of the main text, except here we include our measurement of $\mathrm{Im}[\mathcal{C}]$ for completeness. **b**, Simulated Wigner functions of the maximally-mixed states of GKP qudits.

space, which occur at half lattice spacings (see Figs. S 3,S 8, and S 14). In even dimensions this half lattice spacing is commensurate with the lattice, and when the states mix incoherently the negative peaks get canceled out by the positive peaks from other states. In odd dimensions, however, this half lattice spacing is not commensurate with the lattice, and these negative peaks remain even after incoherent mixing of the states. For our measurement of these mixed states, we opted to perform characteristic function tomography rather than Wigner tomography because of the inherently low contrast of the Wigner function of ρ_d^{mix} for increasing d; achieving the same signal-to-noise ratio with Wigner tomography would have taken a prohibitively long time.

III. CHARACTERIZING QUANTUM MEMORIES

As discussed in the main text, we characterize the performance of our logical GKP qudits as non-binary quantum memories via the average channel fidelity

$$\mathcal{F}_d(\mathcal{E}, I) = \frac{1}{d+1} + \frac{1}{d^2(d+1)} \sum_{n,m=0}^{d-1} \mathrm{Tr}\left[U_{nm}^\dagger \mathcal{E}(U_{nm})\right], \tag{S35}$$

which compares the channel $\mathcal{E}$ to the identity I [22]. Here the U_{nm}'s are elements of a unitary operator basis satisfying the orthogonality relation $\mathrm{Tr}[U_{nm}^\dagger U_{kl}] = \delta_{nk}\delta_{ml} d$, which in our case we take to be the generalized Pauli operators $U_{nm} = X_d^n Z_d^m$ (up to a phase factor, which will be important in our analysis later). Although $\mathcal{F}_d$ will have a complicated time evolution in general, it can always be expanded to short times dt as

$$\mathcal{F}_d(\mathcal{E}, I) \approx 1 - \frac{d-1}{d}\Gamma dt, \tag{S36}$$

where Γ can be interpreted as the effective depolarization rate of the channel $\mathcal{E}$ at short times. This interpretation comes from considering the qudit depolarizing channel

$$\mathcal{E}_{\text{dep}}(\rho) = e^{-\gamma t}\rho + \left(1 - e^{-\gamma t}\right)\frac{I}{d}\text{Tr}[\rho], \tag{S37}$$

which transfers probability from ρ to the maximally-mixed state I/d at rate γ. Note that the factor of $\text{Tr}[\rho] = 1$ is included so this channel is explicitly trace-preserving, even when applied to operators U_{nm} as in Eq. (S35). The average channel fidelity of $\mathcal{E}_{\text{dep}}$ relative to I takes the form

$$\mathcal{F}_d(\mathcal{E}_{\text{dep}}, I) = \frac{1}{d} + \frac{d-1}{d}e^{-\gamma t} \approx 1 - \frac{d-1}{d}\gamma dt, \tag{S38}$$

where in the last step we have expanded the expression to short times dt.

This rate Γ enables us to compare different decay channels on the same footing. In particular, we want to compare the decay rate $\Gamma_d^{\text{logical}}$ of our logical qudit to $\Gamma_d^{\text{physical}}$ of the best physical qudit in our system. We define the QEC gain as their ratio

$$G_d = \Gamma_d^{\text{physical}}/\Gamma_d^{\text{logical}}, \tag{S39}$$

and the break-even point is when this gain is unity.

A. Cavity Fock Qudit

The best physical qudit in our system is the Fock qudit in the cavity, spanned by the states $\{|0\rangle, |1\rangle, ..., |d-1\rangle\}$. The cavity itself decays under both photon loss and dephasing, described by the Kraus operators

$$\begin{aligned} K_0 &= I - \frac{\kappa_{1,c}dt}{2}a^\dagger a - \kappa_{\phi,c}dt(a^\dagger a)^2, \\ K_1 &= \sqrt{\kappa_{1,c}dt}\, a, \\ K_2 &= \sqrt{2\kappa_{\phi,c}dt}\, a^\dagger a, \end{aligned} \tag{S40}$$

where $\kappa_{1,c} = 1/T_{1,c}$ and $\kappa_{\phi,c} = 1/T_{2R,c} - 1/2T_{1,c}$. The overall decay channel of the cavity is then given by

$$\mathcal{E}_c(\rho) = K_0\rho K_0^\dagger + K_1\rho K_1^\dagger + K_2\rho K_2^\dagger. \tag{S41}$$

To express the effective short-time depolarization rate Γ_d^{Fock} of the cavity Fock qudit in terms of $\kappa_{1,c}$ and $\kappa_{\phi,c}$, we truncate the channel $\mathcal{E}_c$ to the first d Fock states, plug into Eq. (S35), expand to lowest order in dt, and compare the result to Eq. (S36). We perform this calculation in Mathematica and obtain

$$\begin{aligned} \Gamma_2^{\text{Fock}} &= \frac{2}{3}\kappa_{1,c} + \frac{2}{3}\kappa_{\phi,c} = (851 \pm 9\ \mu\text{s})^{-1}, \\ \Gamma_3^{\text{Fock}} &= \frac{9}{8}\kappa_{1,c} + \frac{3}{2}\kappa_{\phi,c} = (488 \pm 7\ \mu\text{s})^{-1}, \\ \Gamma_4^{\text{Fock}} &= \frac{8}{5}\kappa_{1,c} + \frac{8}{3}\kappa_{\phi,c} = (332 \pm 6\ \mu\text{s})^{-1}, \end{aligned} \tag{S42}$$

where in the last step we plugged in our measured values for $\kappa_{1,c}$ and $\kappa_{\phi,c}$ (see Table S I).

B. Breaking Down the Average Channel Fidelity

We next analyze the average channel fidelity of our logical GKP qudits by breaking down Eq. (S35) in terms of quantities we can measure experimentally. Our strategy is to partition the set of Pauli operators $\{U_{nm}\}$ into subsets $\{P, P^2, ..., P^{d-1}\}$, where $P \in \{U_{nm}\}$ is assumed to have a non-degenerate spectrum. Since we are free to choose an overall phase factor of our U_{nm}, we may assume without loss of generality that the eigenvalues of P are $1, \omega_d, \omega_d^2, ..., \omega_d^{d-1}$, where $\omega_d = \exp(2\pi i/d)$ is the primitive dth root of unity. The operator P can therefore be spectrally decomposed as

$$P = \sum_{k=0}^{d-1} \omega_d^k |P_k\rangle\langle P_k|, \tag{S43}$$

where $|P_k\rangle$ is the kth eigenket of P satisfying $P|P_k\rangle = \omega_d^k|P_k\rangle$. We can also express the projectors $|P_k\rangle\langle P_k|$ in terms of the operators P^k by considering the expression

$$\begin{aligned}\frac{1}{d}\sum_{\ell=0}^{d-1}\omega_d^{-\ell k}P^\ell =&\frac{1}{d}\sum_{\ell=0}^{d-1}\omega_d^{-\ell k}\sum_{j=0}^{d-1}\omega_d^{\ell j}|P_j\rangle\langle P_j|,\\ =&\frac{1}{d}\sum_{j=0}^{d-1}|P_j\rangle\langle P_j|\sum_{\ell=0}^{d-1}\omega_d^{\ell(j-k)},\\ =&|P_k\rangle\langle P_k|,\end{aligned} \tag{S44}$$

where in the last step we used the identity

$$\sum_{\ell=0}^{d-1}\omega_d^{\ell(j-k)} = d\delta_{jk}. \tag{S45}$$

We next consider terms of the form $\mathrm{Tr}\left[(P^j)^\dagger\mathcal{E}(P^j)\right]$, as appear in Eq. (S35). Using the above results and summing over j, we can write

$$\begin{aligned}\sum_{j=0}^{d-1}\mathrm{Tr}\left[(P^j)^\dagger\mathcal{E}(P^j)\right] &= \sum_{j,k=0}^{d-1}\langle P_k|(P^j)^\dagger\mathcal{E}(P^j)|P_k\rangle,\\ &= \sum_{j,k,\ell,m=0}^{d-1}\omega_d^{j(m-\ell)}\langle P_k|P_\ell\rangle\langle P_\ell|\mathcal{E}(|P_m\rangle\langle P_m|)|P_k\rangle,\\ &= \sum_{j,k,m=0}^{d-1}\omega_d^{j(m-k)}\langle P_k|\mathcal{E}(|P_m\rangle\langle P_m|)|P_k\rangle,\\ &=d\sum_{k=0}^{d-1}\langle P_k|\mathcal{E}(|P_k\rangle\langle P_k|)|P_k\rangle,\end{aligned} \tag{S46}$$

where in the last step we again used Eq. (S45). Finally, we want to remove the contribution of the identity to the left hand side of Eq. (S46). Assuming the steady state of the channel $\mathcal{E}$ is the maximally mixed qudit state, and therefore that $\mathcal{E}(I) = I$, we obtain

$$\sum_{j=1}^{d-1}\mathrm{Tr}\left[(P^j)^\dagger\mathcal{E}(P^j)\right] = -d + d\sum_{k=0}^{d-1}\langle P_k|\mathcal{E}(|P_k\rangle\langle P_k|)|P_k\rangle. \tag{S47}$$

The right hand side of this equation is now in terms of experimentally accessible quantities: the terms in the sum can be measured by preparing the state $|P_k\rangle$, applying the channel $\mathcal{E}$, and measuring the probability that the final state is still $|P_k\rangle$.

C. Average Channel Fidelity for GKP Qubits

In $d = 2$, we partition the set $\{U_{nm}\}$ as

$$\{U_{nm}\} = \{I\}\cup\{X_2\}\cup\{Z_2\}\cup\{\sqrt{\omega_2}X_2Z_2\}, \tag{S48}$$

which is somewhat trivial since each constituent set has only one element, but serves to illustrate our approach nonetheless. We break up Eq. (S35) into sums over each subset of the partition and use Eq. (S47) to obtain the average channel fidelity

$$\mathcal{F}_2(\mathcal{E}, I) = \frac{1}{6}\sum_{P\in\mathcal{P}_2}\sum_{k=0}^{1}\langle P_k|\mathcal{E}(|P_k\rangle\langle P_k|)|P_k\rangle, \tag{S49}$$

where $\mathcal{P}_2 = \{X_2, Z_2, \sqrt{\omega_2}X_2Z_2\}$. Assuming each Pauli eigenstate $|P_k\rangle$ of the GKP qubit decays exponentially toward the maximally mixed state $I/2$ at rate γ_{P_k}, the effective depolarization rate Γ_2^{GKP} can be expressed as

$$\Gamma_2^{\mathrm{GKP}} = \frac{1}{6}\sum_{P\in\mathcal{P}_2}\sum_{k=0}^{1}\gamma_{P_k}, \tag{S50}$$

in agreement with previous work [1].

D. Average Channel Fidelity for GKP Qutrits

In $d = 3$, we partition the set $\{U_{nm}\}$ as

$$\{U_{nm}\} = \{I\} \cup \{X_3, X_3^2\} \cup \{Z_3, Z_3^2\} \cup \{X_3Z_3, X_3^2Z_3^2\} \cup \{X_3^2Z_3, X_3Z_3^2\}. \tag{S51}$$

We again break up Eq. (S35) into sums over each subset of the partition and use Eq. (S47) to obtain the average channel fidelity

$$\mathcal{F}_3(\mathcal{E}, I) = \frac{1}{12}\sum_{P\in\mathcal{P}_3}\sum_{k=0}^{2}\langle P_k|\mathcal{E}(|P_k\rangle\langle P_k|)|P_k\rangle, \tag{S52}$$

where $\mathcal{P}_3 = \{X_3, Z_3, X_3Z_3, X_3^2Z_3\}$. We note that the bases of Pauli operators $P \in \mathcal{P}_3$ form a maximal set of mutually unbiased bases in $d = 3$ [23]. Assuming each Pauli eigenstate $|P_k\rangle$ of the GKP qutrit decays exponentially toward the maximally mixed state $I/3$ at rate γ_{P_k}, the effective depolarization rate Γ_3^{GKP} can be expressed as

$$\Gamma_3^{\mathrm{GKP}} = \frac{1}{12}\sum_{P\in\mathcal{P}_3}\sum_{k=0}^{2}\gamma_{P_k}. \tag{S53}$$

E. Average Channel Fidelity for GKP Ququarts

In $d = 4$ the situation is more complex, since $\{U_{nm}\}$ can't be partitioned into disjoint subsets $\{P, P^2, ..., P^{d-1}\}$. The best we can do is

$$\begin{aligned}\{U_{nm}\} = \{I\} &\cup \{X_4, X_4^2, X_4^3\}\\ &\cup \{Z_4, Z_4^2, Z_4^3\}\\ &\cup \{\sqrt{\omega_4}X_4Z_4, \omega_4X_4^2Z_4^2, \omega_4^{3/2}X_4^3Z_4^3\}\\ &\cup \{X_4^2Z_4, Z_4^2, X_4^2Z_4^3\}\\ &\cup \{\sqrt{\omega_4}X_4^3Z_4, \omega_4X_4^2Z_4^2, \omega_4^{3/2}X_4Z_4^3\}\\ &\cup \{X_4Z_4^2, X_4^2, X_4^3Z_4^2\}.\end{aligned} \tag{S54}$$

If we apply the same procedure here as in $d = 2$ and $d = 3$ we would end up double-counting the contribution of Pauli operators X_4^2, Z_4^2, and $X_4^2Z_4^2$ to Eq. (S35). As it turns out, however, $[X_4^2, Z_4^2] = 0$, so all three of these operators can be simultaneously diagonalized, enabling us to effectively subtract off the effect of this double counting. To this end, we introduce what we call the ququart parity basis $\{|\pm, n\rangle_4 : n = 0, 1\}$, which are the simultaneous eigenstates of X_4^2 and Z_4^2 according to

$$\begin{aligned}X_4^2|\pm, n\rangle_4 &= \pm|\pm, n\rangle_4,\\ Z_4^2|\pm, n\rangle_4 &= (-1)^n|\pm, n\rangle_4.\end{aligned} \tag{S55}$$

Using the spectral decomposition of the operators in $\mathcal{P}_{\text{parity}} = \{X_4^2, Z_4^2, X_4^2 Z_4^2\}$

$$
\begin{aligned}
X_4^2 &= \sum_{\substack{s=\pm\\ n=0,1}} s|s,n\rangle\langle s,n|,\\
Z_4^2 &= \sum_{\substack{s=\pm\\ n=0,1}} (-1)^n|s,n\rangle\langle s,n|,\\
X_4^2 Z_4^2 &= \sum_{\substack{s=\pm\\ n=0,1}} s(-1)^n|s,n\rangle\langle s,n|,
\end{aligned}
\tag{S56}
$$

we can calculate

$$
\begin{aligned}
\sum_{P\in\mathcal{P}_{\text{parity}}} \operatorname{Tr}\left[P^\dagger \mathcal{E}(P)\right] &= \sum_{\substack{s,t=\pm\\ n,m=0,1}} \left(st + st(-1)^{n+m} + (-1)^{n+m}\right)\langle s,n|\mathcal{E}(|t,m\rangle\langle t,m|)|s,n\rangle,\\
&= -4 + \sum_{\substack{s,t=\pm\\ n,m=0,1}} \left(1 + st + st(-1)^{n+m} + (-1)^{n+m}\right)\langle s,n|\mathcal{E}(|t,m\rangle\langle t,m|)|s,n\rangle,\\
&= -4 + 4\sum_{\substack{s=\pm\\ n=0,1}} \langle s,n|\mathcal{E}(|s,n\rangle\langle s,n|)|s,n\rangle,
\end{aligned}
\tag{S57}
$$

where in the last step we used $1 + st + st(-1)^{n+m} + (-1)^{n+m} = 4\delta_{nm}\delta_{st}$ for $s,t\in\{-1,1\}$ and $n,m\in\{0,1\}$. We can now once again break up Eq. (S35) into sums over each subset of the non-disjoint partition from Eq. (S54), evaluate these sums using Eq. (S47), and subtract off the contribution of the set $\mathcal{P}_{\text{parity}}$ that is double-counted due to the non-disjointness of the partitioning. Doing so, we obtain the average channel fidelity

$$
\mathcal{F}_4(\mathcal{E}, I) = \frac{1}{20}\left[\sum_{P\in\mathcal{P}_4}\sum_{k=0}^{3}\langle P_k|\mathcal{E}\left(|P_k\rangle\langle P_k|\right)|P_k\rangle - \sum_{\substack{s=\pm\\ n=0,1}} \langle s,n|\mathcal{E}\left(|s,n\rangle\langle s,n|\right)|s,n\rangle\right].
\tag{S58}
$$

Finally, if each Pauli eigenstate $|P_k\rangle$ (parity eigenstate $|\pm,n\rangle$) of the GKP ququart decays exponentially to the maximally mixed state $I/4$ at rate γ_{P_k} ($\gamma_{\pm,n}$), the effective depolarization rate Γ_4^{GKP} can be expressed as

$$
\Gamma_4^{\text{GKP}} = \frac{1}{20}\left[\sum_{P\in\mathcal{P}_4}\sum_{k=0}^{3}\gamma_{P_k} - \sum_{\substack{s=\pm\\ n=0,1}} \gamma_{\pm,n}\right].
\tag{S59}
$$

IV. LOGICAL GKP QUBIT

In this section we present the methods and results pertaining to our experimental realization of a logical GKP qubit beyond break-even, using established techniques from prior work on GKP qubits [1, 16, 24, 25]. Our goal is to provide a basis of comparison with our novel techniques and results for the GKP qutrit and ququart.

A. State Preparation

To prepare the Pauli eigenstates of the GKP qubit defined in Table S II, we use interleaved sequences of ECD gates and ancilla qubit rotations [12], as described in Sec. I B. We optimize depth 8 ECD circuits for each state with envelope size $\Delta = 0.34$, approximated numerically using the method described in Sec. II. To verify that we are preparing the desired states, we run these ECD circuits experimentally and perform Wigner tomography of the prepared states, the results of which are presented in Fig. S 3. We then reconstruct the density matrices ρ_{prep} of the prepared states from their measured Wigner functions and compute their fidelity with respect to the target states $|\psi_{\text{target}}\rangle$ according to $\mathcal{F}_{\text{prep}} = \langle\psi_{\text{target}}|\rho_{\text{prep}}|\psi_{\text{target}}\rangle$, the results of which are presented in Table S III.

B. Pauli Measurements

Following previous work [16, 24, 26], we measure the GKP qubit in the basis of Pauli operator P_2 by initializing the ancilla in the $|+\rangle$ state and performing a controlled-Pauli operation CP_2. If the GKP qubit starts out in state $|\psi\rangle_2 = c_0|P_0\rangle_2 + c_1|P_1\rangle_2$, then this operation entangles the two systems as

$$CP_2|+\rangle|\psi\rangle_2 = c_0|+\rangle|P_0\rangle_2 + c_1|+\rangle|P_1\rangle_2, \tag{S60}$$

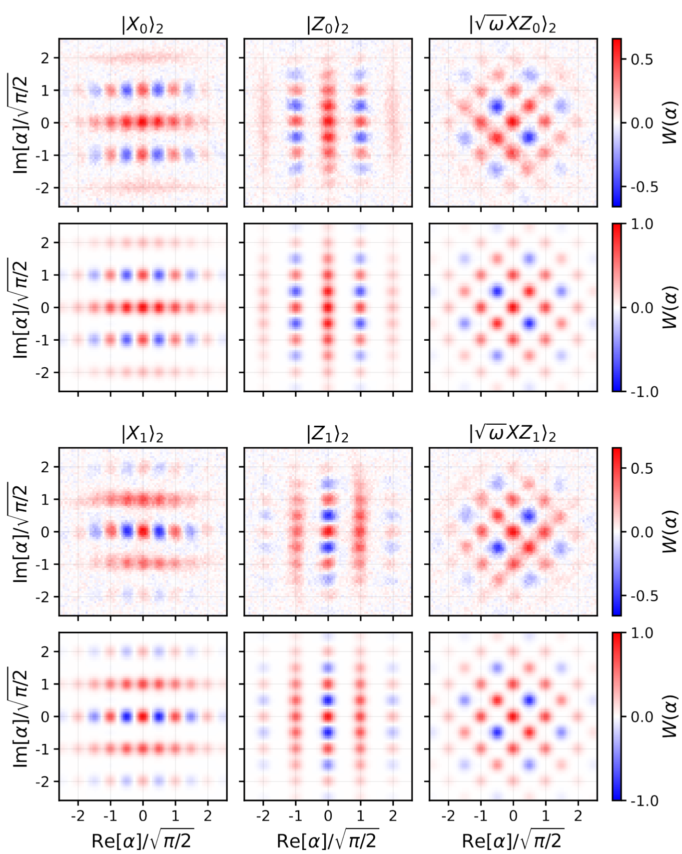

FIG. S 3. **GKP qubit state preparation.** For each state, the measured Wigner function of the prepared state is on top, and that of the target state is on the bottom. We use depth 8 ECD circuits and a finite-energy envelope size $\Delta = 0.34$.

$\mathcal{F}_{\text{prep}}$ (%)	$\lvert X_n\rangle_2$	$\lvert Z_n\rangle_2$	$\lvert\sqrt{\omega}XZ_n\rangle_2$
$n=0$	90	88	89
$n=1$	89	89	90

Table S III. Fidelity $\mathcal{F}_{\text{prep}} = \langle\psi_{\text{target}}|\rho_{\text{prep}}|\psi_{\text{target}}\rangle$ of prepared Pauli eigenstates of the GKP qubit, determined by reconstructing the prepared state from its measured Wigner function and comparing it to the target state.

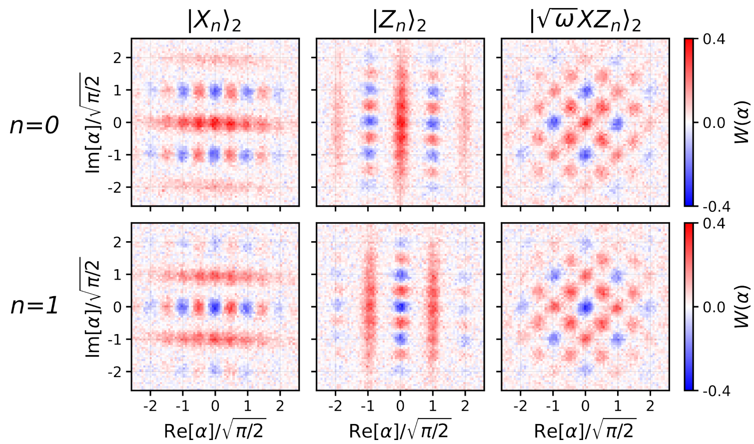

FIG. S 4. **GKP qubit Pauli measurement backaction.** In each column, we implement a projective measurement with respect to the indicated basis and then perform Wigner tomography post-selected on the measurement outcomes.

such that a subsequent measurement of the ancilla along its x axis constitutes a measurement of the GKP qubit in the basis of P_2, and collapses the state accordingly. In this work we use CP_d operations designed for the ideal GKP code, which incur infidelity when applied to the finite-energy code. In the case of GKP qubits these CP_2 gates have been adapted to the finite-energy code [19, 25, 27] but we choose not to use them in the present work, in the interest of comparison with the techniques we develop for the GKP qutrit and ququart. For $P_2 \in \{X_2, Z_2, \sqrt{\omega}X_2Z_2\}$, we compile the controlled Pauli gate CP_2 in terms of an ECD gate and ancilla rotations according to

$$\begin{aligned} CX_2 =& D(\sqrt{\pi/2}/2)\text{ECD}(\sqrt{\pi/2})\sigma_x, \\ CZ_2 =& D(i\sqrt{\pi/2}/2)\text{ECD}(i\sqrt{\pi/2})\sigma_x, \\ C(\sqrt{\omega}X_2Z_2) =& D(e^{i\pi/4}\sqrt{\pi}/2)\text{ECD}(e^{i\pi/4}\sqrt{\pi})\sigma_x, \end{aligned} \tag{S61}$$

as described in the Methods section of the main text. In our experiments we do not implement the unconditional displacements $D(\beta_{nm}/2)$, which means that our measurement sequence will apply an overall displacement $D(-\beta_{nm}/2)$ that brings us out of the code space. However, it also means that the envelope of our finite-energy code remains centered, since our conditional displacements are symmetric about the origin.

To verify that our logical Pauli measurements work as intended, we prepare the maximally mixed state of the GKP qubit ρ_2^{mix} by performing 160 rounds of sBs starting from the cavity in vacuum, implement the CP_2 gate, measure the ancilla along its x axis, and perform Wigner tomography of the cavity post-selected on outcome of this measurement. The results of this experiment are shown in Fig. S 4, from which we can see that the Pauli measurement works as we expect: it projects onto the Pauli eigenstate $|P_n\rangle_2$ according to the measurement result, and implements a $D(-\beta_{nm}/2)$ operation on the underlying ideal GKP codewords while leaving the finite-energy envelope centered.

C. Optimized Qubit Beyond Break-even

We optimize the QEC protocol of the GKP qubit using a reinforcement learning (RL) agent [28] following the method described in Ref. [1] (also, see the Methods section of the main text). In Fig. S 5 we present both the reward signal and key parameters of the sBs circuit as a function of training epoch. Our interpretation is that the RL training serves three main purposes [1]. First, it enables us to go beyond the constraints imposed by our model for

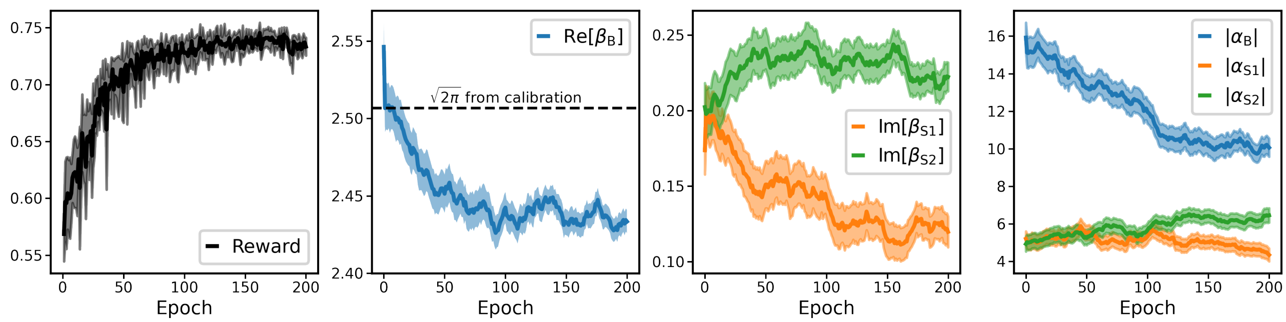

FIG. S 5. **GKP qubit RL training.** Lines indicate mean values while the shaded regions indicate the one-standard-deviation confidence interval.

the QEC protocol (for example, finding a better strategy where the second small conditional displacement amplitude $|\beta_{S2}|$ of the sBs protocol is greater than $|\beta_{S1}|$ of the first). Second, it mitigates experimental imperfections that are difficult to model (for example, finding intermediate displacement amplitudes $|\alpha_{S1,B,S2}|$ that avoid bringing spurious two-level-systems onto resonance with our ancilla qubit). Third, it performs a meta-calibration of all pulse parameters in the midst of the complicated control sequences required for QEC (for example, finding a 3% deviation between $|\beta_B|$ and $\sqrt{2\pi}$, and finding optimal DRAG parameters [29] for each ancilla qubit pulse). The total duration of each sBs round is constrained to be 7 μs; the optimal protocol found by the RL training spends 3632 ns measuring and resetting the ancilla qubit, 1792 ns performing the sBs protocol, 1352 ns idling, and 224 ns executing FPGA sequencing instructions.

To evaluate the average channel fidelity of the optimal QEC protocol via Eq. (S49), we measure the probabilities $\langle P_n|\mathcal{E}^N_{\rm opt}(|P_n\rangle\langle P_n|)|P_n\rangle_2$ as a function of N for $n = 0, 1$ and $P \in \mathcal{P}_2 = \{X_2, Z_2, \sqrt{\omega}X_2Z_2\}$, where $\mathcal{E}^N_{\rm opt}$ is the channel corresponding to N rounds of the optimal QEC protocol. We measure these probabilities by preparing state $|P_n\rangle$, performing N rounds of QEC with the optimal protocol (sweeping the value of N), and measuring the GKP qubit in the basis of Pauli operator P. The results of these six experiments are presented in Fig. S 6. We then fit each probability $\langle P_n|\mathcal{E}^N_{\rm opt}(|P_n\rangle\langle P_n|)|P_n\rangle_2$ to an exponential decay and find the decay rate γ_{P_n}. Note that we neglect the first data point of these measurements, due to an artifact resulting from imperfect state preparation. These rates γ_{P_n} enable us to calculate the effective short-time depolarization rate of the optimized logical GKP qubit

$$\Gamma_2^{\rm GKP} = (1537 \pm 12\,\mu{\rm s})^{-1}\,, \tag{S62}$$

using Eq. (S50). Comparing with $\Gamma_2^{\rm Fock} = (851 \pm 9\,\mu{\rm s})^{-1}$, we obtain a QEC gain of

$$G_2 = \Gamma_2^{\rm Fock}/\Gamma_2^{\rm GKP} = 1.81 \pm 0.02, \tag{S63}$$

well beyond the break-even point. There are several possible reasons why this result is worse than the factor of 2.3 previously reported for the same device [1]. First, we reclamped the chip containing the transmon, leading to lower transmon thermal population, less storage dephasing, a smaller $\Gamma_2^{\rm Fock}$, and thus a smaller G_2. Second, this reclamping and thermal cycling of the device likely changed the bath of two-level-systems coupling to the transmon [30, 31]. Third, we use a longer sBs duration of 7 μs that may be suboptimal.

Lastly, we find the effective envelope size of our optimal GKP qubit by measuring its steady-state characteristic function $\mathcal{C}(\beta)$ near the origin of reciprocal phase space. In this experiment we run the optimal protocol for 500 rounds followed by characteristic function tomography, the result of which is shown in Fig. S 7. We fit the real part of the characteristic function to a Gaussian according to $\mathrm{Re}[\mathcal{C}(\beta)] = A\exp\left(-|\beta|^2/2\Delta_{\rm eff}^2\right) + B$, and find $\Delta_{\rm eff} = 0.290 \pm 0.001$. This is not exactly the same thing as the envelope size, since $\Delta_{\rm eff}$ will be affected by population in error spaces, such as photon-loss and photon-gain acting on the code space [1]. More precisely, this measurement of the characteristic function near the origin of reciprocal phase space enables us to calculate photon statistics of the state [15] (see Sec. I C). For Gaussian $\mathrm{Re}[\mathcal{C}(\beta)]$ and null $\mathrm{Im}[\mathcal{C}(\beta)]$, we have $\langle a^\dagger a\rangle = (1/\Delta_{\rm eff}^2 - 1)/2 = 5.45 \pm 0.04$ photons.

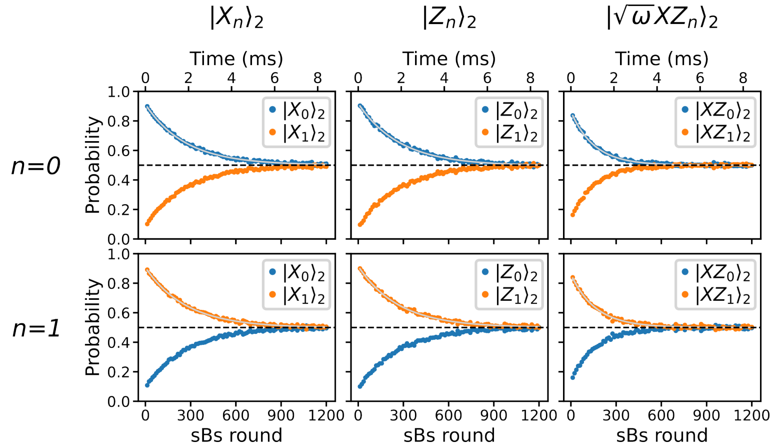

$\gamma_{P_n}^{-1}$ (μs)	$\lvert X_n\rangle_2$	$\lvert Z_n\rangle_2$	$\lvert\sqrt{\omega}XZ_n\rangle_2$
$n=0$	1863 ± 27	1935 ± 35	1086 ± 19
$n=1$	1902 ± 28	1872 ± 32	1150 ± 25

FIG. S 6. **Lifetime of the optimized logical GKP qubit.** The solid grey lines are fits to an exponential decay. The dashed black line indicates a probability of 1/2.

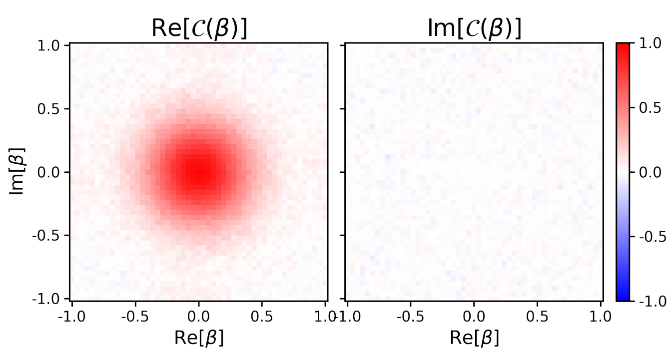

FIG. S 7. Steady-state characteristic function of the optimal GKP qubit QEC protocol, sampled near the origin of reciprocal phase space.

V. LOGICAL GKP QUTRIT

In this section we present the methods and results pertaining to our experimental realization of a logical GKP qutrit ($d = 3$) beyond break-even.

A. State Preparation

To prepare the Pauli eigenstates of the GKP qutrit defined in Table S II, we again use interleaved sequences of ECD gates and ancilla qubit rotations [12], as described in Sec. I B. We optimize depth 8 ECD circuits for each state with envelope size $\Delta = 0.32$, approximated numerically using the method described in Sec. II. To verify that we are preparing the desired states, we run these ECD circuits experimentally and perform Wigner tomography of the prepared states, the results of which are presented in Fig. S 8. We then reconstruct the density matrices ρ_{prep} of the prepared states from their measured Wigner functions and compute their fidelity with respect to the target states $|\psi_{\text{target}}\rangle$ according to $\mathcal{F} = \langle\psi_{\text{target}}|\rho_{\text{prep}}|\psi_{\text{target}}\rangle$, the results of which are presented in Table S IV.

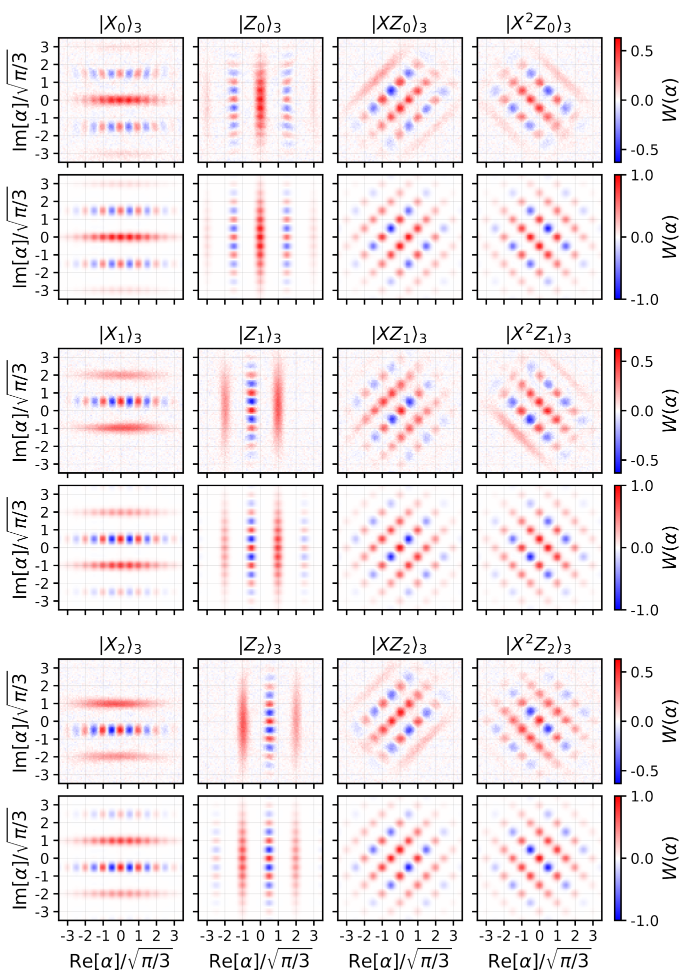

FIG. S 8. **GKP Qutrit state preparation.** For each state, the measured Wigner function of the prepared state is on top, and that of the target state is on the bottom. We use depth 8 ECD circuits and a finite-energy envelope size $\Delta = 0.32$.

$\mathcal{F}_{\text{prep}}$ (%)	$\lvert X_n\rangle_3$	$\lvert Z_n\rangle_3$	$\lvert XZ_n\rangle_3$	$\lvert X^2Z_n\rangle_3$
$n=0$	86	85	85	74
$n=1$	85	86	81	85
$n=2$	87	84	83	82

Table S IV. Fidelity $\mathcal{F}_{\text{prep}} = \langle\psi_{\text{target}}|\rho_{\text{prep}}|\psi_{\text{target}}\rangle$ of prepared Pauli eigenstates of the GKP qutrit, determined by reconstructing the prepared state from its measured Wigner function and comparing it to the target state.

B. Pauli Measurements

To measure our GKP qutrit in the basis of Pauli operator P_3 we devised the two-part circuit depicted in Fig. 2b of the main text, which measures the state of our logical three-level system via two binary measurements of our ancilla. If the GKP qutrit starts out in state $|\psi\rangle_3 = c_0|P_0\rangle_3 + c_1|P_1\rangle_3 + c_2|P_2\rangle_3$ and the ancilla starts out in state $|+\rangle$, then the first part of the circuit entangles the two systems as

$$R^\dagger_{\pi/2}(\pi/2)\ CP_3\ R^\dagger_0(\theta_0)\ CP_3^\dagger\ R_0(\theta_0)\ CP_3\ |+\rangle|\psi_3\rangle = c_0|g\rangle|P_0\rangle_3 + e^{-i\theta_0/2}|e\rangle\Big(c_1|P_1\rangle_3 - c_2|P_2\rangle_3\Big), \tag{S64}$$

where $\theta_0 = 2\arctan\big(1/\sqrt{2}\big)$, such that a subsequent measurement of the ancilla along its z axis constitutes a projective measurement on the qutrit distinguishing between the $|P_0\rangle_3$ state and the $\{|P_1\rangle_3, |P_2\rangle_3\}$ subspace. Similarly, the second part of the circuit entangles the two systems as

$$R^\dagger_{7\pi/6}(\pi/2)\ CP_3\ R^\dagger_0(\theta_0)\ CP_3^\dagger\ R_{2\pi/3}(\theta_0)\ CP_3\ |+\rangle|\psi_3\rangle = c_1|g\rangle|P_1\rangle_3 + e^{-i\theta_0/2}e^{2\pi i/3}|e\rangle\Big(c_0|P_0\rangle_3 + c_2|P_2\rangle_3\Big), \tag{S65}$$

such that a subsequent measurement of the ancilla along its z axis constitutes a projective measurement on the qutrit distinguishing between the $|P_1\rangle_3$ state and the $\{|P_0\rangle_3, |P_2\rangle_3\}$ subspace. Performing these two measurements sequentially therefore projects the qutrit onto one of the three states, with probabilities determined by the initial amplitudes $\{c_0, c_1, c_2\}$. Note that the relative phases accumulated between the states $|P_n\rangle_3$ do not affect the overall projective measurement.

Experimentally, we find that for finite-energy GKP qutrits the fidelity of this measurement scheme depends on the state $|P_n\rangle_3$. To mitigate this effect we symmetrize the measurement by adding a geometric phase to the ancilla via a $\sigma_z(2\pi k/3)$ gate after every CP_3 operation (and a $\sigma_z(-2\pi k/3)$ gate after every $CP_3^\dagger$ operation), where we call k the symmetrization index. This modifies the measurement circuit such that the first part distinguishes between $|P_k\rangle_3$ and the subspace $\{|P_{n\neq k}\rangle_3\}$, and the second part distinguishes between $|P_{k+1}\rangle_3$ and the subspace $\{|P_{n\neq k+1}\rangle_3\}$. For all the GKP qutrit Pauli measurements presented in this work, we average this measurement scheme over $k = 0, 1, 2$.

For $P_3 \in \{X_3, Z_3, X_3Z_3, X_3^2Z_3\}$, we compile the controlled Pauli gate CP_3 in terms of an ECD gate and ancilla rotations according to

$$\begin{aligned}
CX_3 =& D(\sqrt{\pi/3}/2)\ \mathrm{ECD}(\sqrt{\pi/3})\ \sigma_x,\\
CZ_3 =& D(i\sqrt{\pi/3}/2)\ \mathrm{ECD}(i\sqrt{\pi/3})\ \sigma_x,\\
CX_3Z_3 =& D(e^{i\pi/4}\sqrt{2\pi/3}/2)\ \sigma_z(-\pi/3)\ \mathrm{ECD}(e^{i\pi/4}\sqrt{2\pi/3})\ \sigma_x,\\
CX_3^2Z_3 =& D(e^{3\pi i/4}\sqrt{2\pi/3}/2)\ \sigma_z(\pi/3)\ \mathrm{ECD}(e^{3\pi i/4}\sqrt{2\pi/3})\ \sigma_x,
\end{aligned} \tag{S66}$$

as described in the Methods section of the main text. In our experiments we do not implement the unconditional displacements $D(\beta_{nm}/2)$ associated with each CP_3, but here they all commute through the entire circuit so their combined effect can be considered at the end of the two-part circuit. This means that our measurement sequence will apply an overall displacement $D(-\beta_{nm})$ that keeps us in the code space and has no effect on the measurement outcomes.

To verify that our logical Pauli measurements work as intended, we prepare the maximally mixed state of the GKP qutrit ρ_3^{mix} by performing 200 rounds of sBs starting from the cavity in vacuum, implement the two-part measurement circuit, and perform Wigner tomography of the cavity post-selected on the outcomes of the two binary measurements. The results of this experiment are shown in Fig. S 9, from which we can see that the Pauli measurement works as we

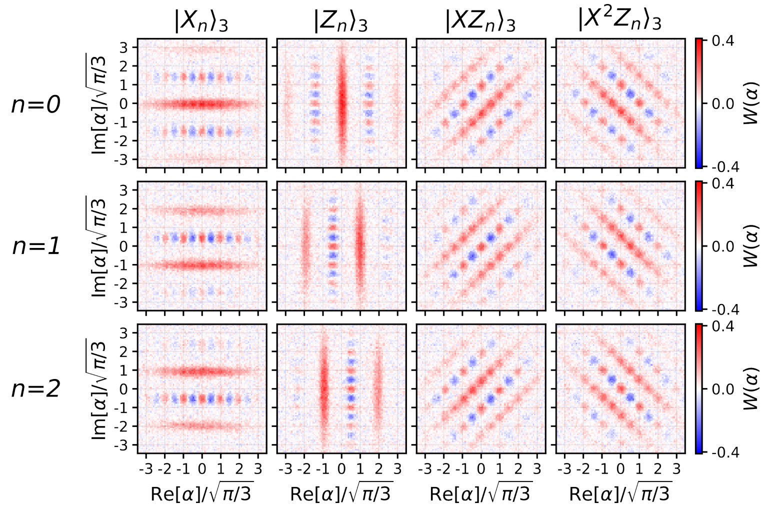

FIG. S 9. **GKP qutrit Pauli measurement backaction.** In each column, we implement a projective measurement with respect to the indicated basis and then perform Wigner tomography post-selected on the measurement outcomes.

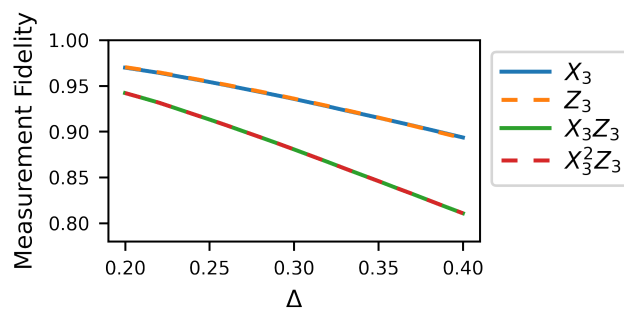

FIG. S 10. GKP qutrit Pauli measurement fidelity (simulation).

expect: it projects onto the Pauli eigenstate $|P_n\rangle_3$ according to measurement result, maintaining its centered envelope and remaining in the codespace.

We simulate the fidelity of these logical Pauli measurements on the qutrit by preparing eigenstate $|P_n\rangle_3$ with finite-energy envelope size Δ, performing the Pauli measurement in the basis of P_3, and finding the probability $p(P_n|P_n)$ that we measure state $|P_n\rangle_3$ at the end. We quantify the average measurement fidelity by

$$\mathcal{F}_{P_3} = \frac{1}{3}\left[p(P_0|P_0) + p(P_1|P_1) + p(P_2|P_2)\right]. \tag{S67}$$

The results of this simulation as a function of Δ are shown in Fig. S 10. As noted in the main text, these measurements are designed for the ideal code, leading to limited fidelity when applied to finite-energy codewords. We expect it is possible to adapt these measurements to the finite-energy case [19, 25, 27, 32], but we leave this for future work.

C. Optimized Qutrit Beyond Break-even

We optimize the QEC protocol of the GKP qutrit using a reinforcement learning (RL) agent [28] following the method described in Ref. [1] (also, see the Methods section of the main text). In Fig. S 11 we present both the reward signal and key parameters of the sBs circuit as a function of training epoch. For our interpretation of these results, see our discussion in Sec. IV C. The total duration of each sBs round is constrained to be 7 μs; the optimal protocol found by the RL training spends 3632 ns measuring and resetting the ancilla qubit, 1808 ns performing the sBs protocol, 1336 ns idling, and 224 ns executing FPGA sequencing instructions.

To evaluate the average channel fidelity of the optimal QEC protocol via Eq. (S52), we measure the probabilities $\langle P_n|\mathcal{E}^N_{\rm opt}(|P_n\rangle\langle P_n|)|P_n\rangle_3$ as a function of N for $n = 0, 1, 2$ and $P \in \mathcal{P}_3 = \{X_3, Z_3, X_3Z_3, X_3^2Z_3\}$, where $\mathcal{E}^N_{\rm opt}$ is the channel corresponding to N rounds of the optimal QEC protocol. We measure these probabilities by preparing state

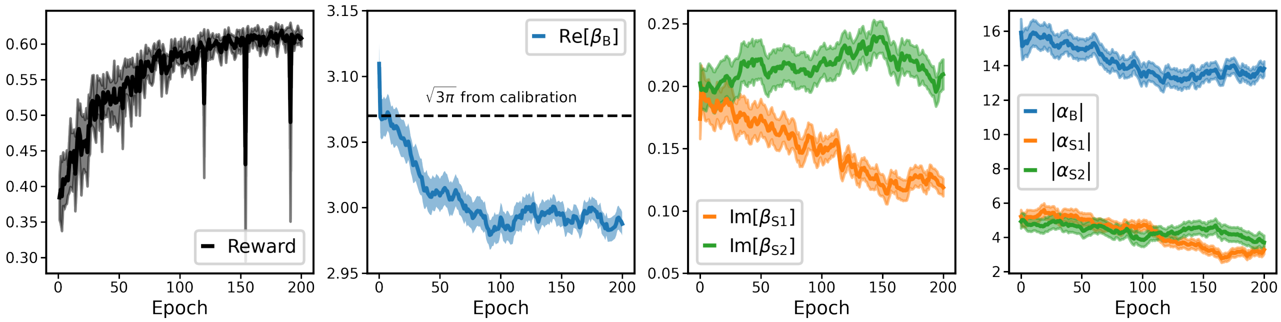

FIG. S 11. **GKP qutrit RL training.** Lines indicate mean values while the shaded regions indicate the one-standard-deviation confidence interval.

$|P_n\rangle$, performing N rounds of QEC with the optimal protocol (sweeping the value of N), and measuring the GKP qutrit in the basis of Pauli operator P. The results of these twelve experiments are presented in Fig. S 12. We then fit each probability $\langle P_n|\mathcal{E}^N_{\rm opt}(|P_n\rangle\langle P_n|)|P_n\rangle_3$ to an exponential decay and find the decay rate γ_{P_n}. Note that we neglect the first data point of these measurements, due to an artifact resulting from imperfect state preparation. These rates γ_{P_n} enable us to calculate the effective short-time depolarization rate of the optimized logical GKP qutrit

$$\Gamma_3^{\rm GKP} = (886 \pm 3\,\mu{\rm s})^{-1}\,, \tag{S68}$$

using Eq. (S53). Comparing with $\Gamma_3^{\rm Fock} = (488 \pm 7\,\mu{\rm s})^{-1}$, we obtain a QEC gain of

$$G_3 = \Gamma_3^{\rm Fock}/\Gamma_3^{\rm GKP} = 1.82 \pm 0.03, \tag{S69}$$

well beyond the break-even point.

Lastly, we find the effective envelope size of our optimal GKP qutrit by measuring its steady-state characteristic function $\mathcal{C}(\beta)$ near the origin of reciprocal phase space. In this experiment we run the optimal protocol for 400 rounds followed by characteristic function tomography, the result of which is shown in Fig. S 13. From this measurement we find an effective envelope size $\Delta_{\rm eff} = 0.261 \pm 0.001$, corresponding to average photon number $\langle a^\dagger a\rangle = (1/\Delta^2_{\rm eff} - 1)/2 = 6.85 \pm 0.06$. For more context on this analysis, see our discussion in Sec. IV C.

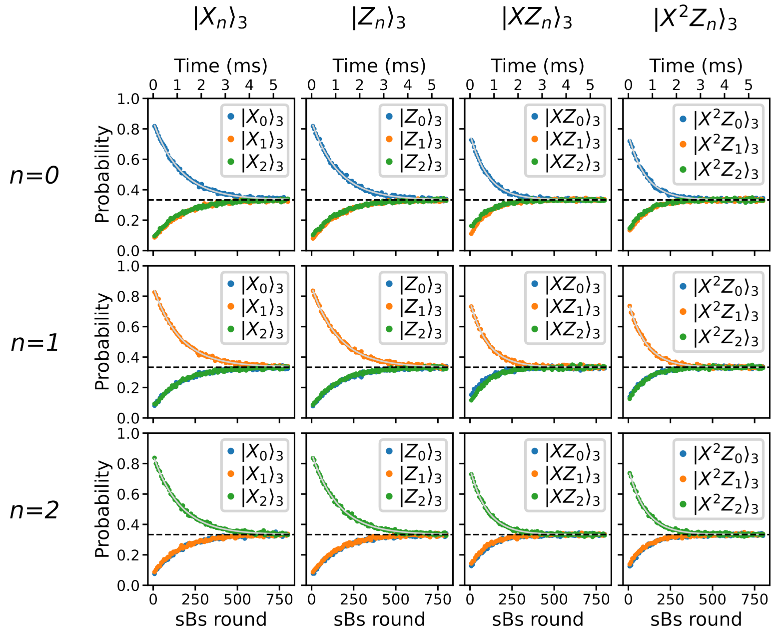

$\gamma_{P_n}^{-1}$ (μs)	$\lvert X_n\rangle_3$	$\lvert Z_n\rangle_3$	$\lvert XZ_n\rangle_3$	$\lvert X^2Z_n\rangle_3$
$n=0$	1153 ± 13	1120 ± 15	743 ± 10	727 ± 11
$n=1$	1117 ± 12	1138 ± 14	737 ± 11	731 ± 11
$n=2$	1120 ± 14	1107 ± 14	720 ± 10	723 ± 11

FIG. S 12. **Lifetime of the optimized GKP qutrit.** The solid grey lines are fits to an exponential decay. The dashed black line indicates a probability of 1/3.

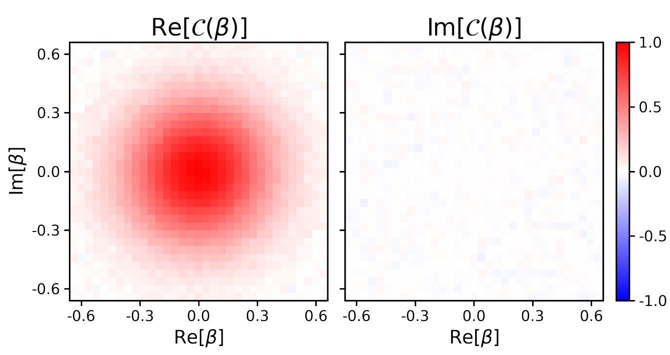

FIG. S 13. Steady-state characteristic function of the optimal GKP qutrit QEC protocol, sampled near the origin of reciprocal phase space.

VI. LOGICAL GKP QUQUART

In this section we present the methods and results pertaining to our experimental realization of a logical GKP ququart ($d = 4$) beyond break-even.

A. State Preparation

To prepare the Pauli eigenstates and parity states of the GKP ququart defined in Table S II, we again use interleaved sequences of ECD gates and ancilla qubit rotations [12], as described in Sec. I B. We optimize depth 8 ECD circuits for each state with envelope size $\Delta = 0.32$, approximated numerically using the method described in Sec. II. To verify that we are preparing the desired states, we run these ECD circuits experimentally and perform Wigner tomography of the prepared states, the results of which are presented in Fig. S 14. We then reconstruct the density matrices ρ_{prep} of the prepared states from their measured Wigner functions and compute their fidelity with respect to the target states $|\psi_{\text{target}}\rangle$ according to $\mathcal{F} = \langle\psi_{\text{target}}|\rho_{\text{prep}}|\psi_{\text{target}}\rangle$, the results of which are presented in Table S V.

B. Pauli and Parity Measurements

To measure our GKP ququart in the basis of Pauli operator P_4 we devised the two-part circuit depicted in Fig. 3b of the main text, which measures the state of our logical four-level system via two binary measurements of our ancilla. This is a simpler measurement than the case of the qutrit, since sequential binary measurements are more natural for a 2^n dimensional system. If the GKP ququart starts out in state $|\psi\rangle_4 = c_0|P_0\rangle_4 + c_1|P_1\rangle_4 + c_2|P_2\rangle_4 + c_3|P_3\rangle_4$ and the ancilla starts out in state $|+\rangle$, then the first part of the circuit entangles the two systems as

$$CP_4^2|+\rangle|\psi\rangle_4 = |+\rangle\Big(c_0|P_0\rangle_4 + c_1|P_1\rangle_4\Big) + |-\rangle\Big(c_2|P_2\rangle_4 + c_3|P_3\rangle_4\Big), \tag{S70}$$

such that a subsequent measurement of the ancilla along its x axis constitutes a projective measurement on the ququart distinguishing between the even subspace $\{|P_0\rangle_4, |P_2\rangle_4\}$ and the odd subspace $\{|P_1\rangle_4, |P_3\rangle_4\}$. Depending on the measurement result, our post-measurement state is given by one of the two states

$$\begin{aligned} |\psi_{\text{even}}\rangle_4 =& \frac{1}{\sqrt{|c_0|^2 + |c_2|^2}}\Big(c_0|P_0\rangle_4 + c_2|P_2\rangle_4\Big), \\ |\psi_{\text{odd}}\rangle_4 =& \frac{1}{\sqrt{|c_1|^2 + |c_3|^2}}\Big(c_1|P_1\rangle_4 + c_3|P_3\rangle_4\Big). \end{aligned} \tag{S71}$$

$\mathcal{F}_{\text{prep}}$ (%)	$\lvert X_n\rangle_4$	$\lvert Z_n\rangle_4$	$\lvert\sqrt{\omega}XZ_n\rangle_4$	$\lvert X^2Z_n\rangle_4$	$\lvert\sqrt{\omega}X^3Z_n\rangle_4$	$\lvert XZ_n^2\rangle_4$
$n = 0$	92	89	87	87	87	88
$n = 1$	94	83	89	89	93	91
$n = 2$	93	85	88	85	91	90
$n = 3$	86	92	89	89	86	91

$\mathcal{F}_{\text{prep}}$ (%)	
$\lvert +,0\rangle_4$	83
$\lvert -,0\rangle_4$	90
$\lvert +,1\rangle_4$	74
$\lvert -,1\rangle_4$	84

Table S V. Fidelity $\mathcal{F}_{\text{prep}} = \langle\psi_{\text{target}}|\rho_{\text{prep}}|\psi_{\text{target}}\rangle$ of prepared Pauli eigenstates and parity states of the GKP ququart, determined by reconstructing the prepared state from its measured Wigner function and comparing it to the target state.

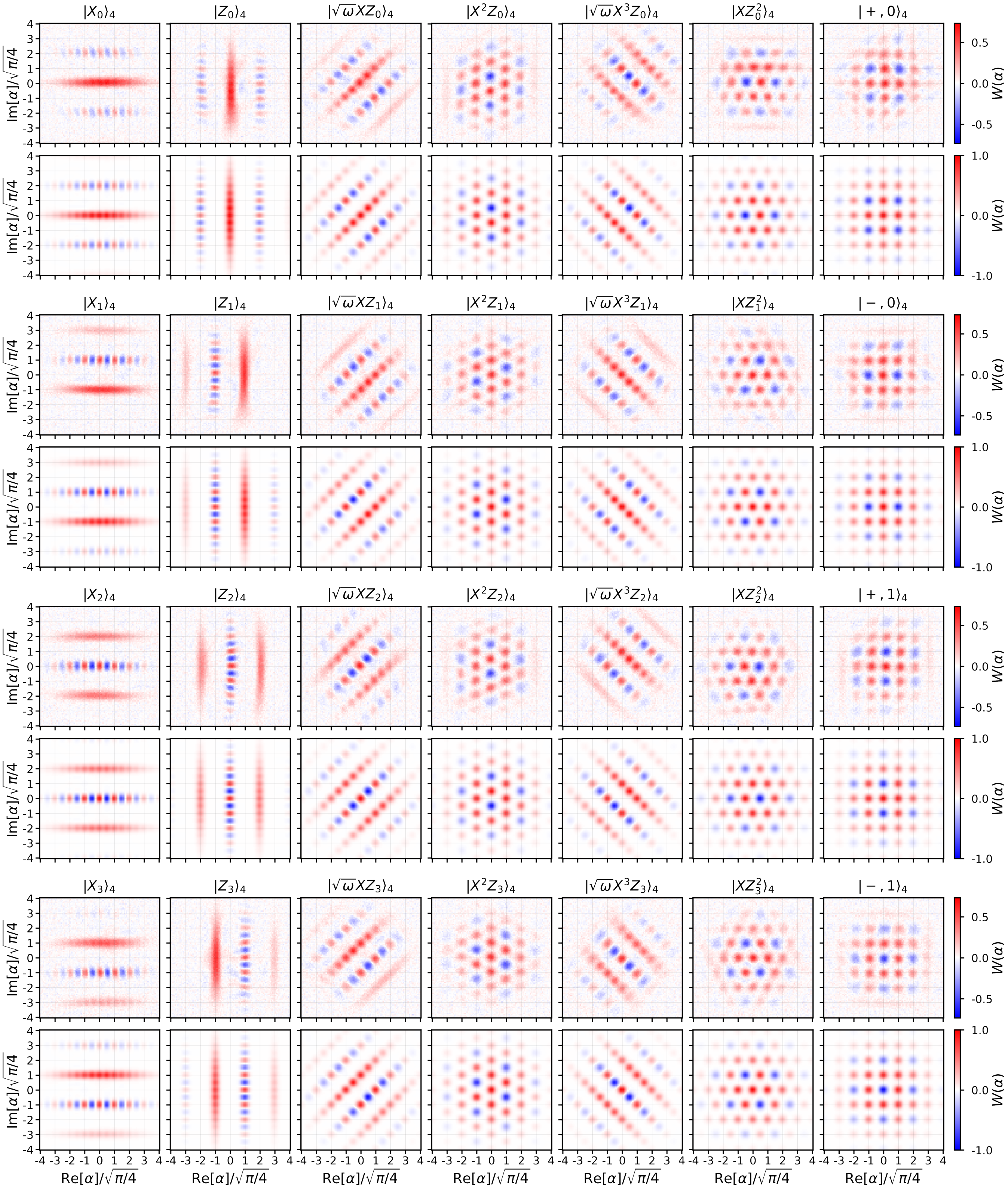

FIG. S 14. **GKP ququart state preparation.** For each state, the measured Wigner function of the prepared state is on top, and that of the target state is on the bottom. We use depth 8 ECD circuits and a finite-energy envelope size $\Delta = 0.32$.

Starting from these states, and the ancilla reinitialized in the $|+\rangle$ state, the second part of the measurement circuit entangles the two systems according to

$$\begin{aligned} CP_4|+\rangle|\psi_{\text{even}}\rangle_4 =& \frac{1}{\sqrt{|c_0|^2+|c_2|^2}}\Big(c_0|+\rangle|P_0\rangle_4 + c_2|-\rangle|P_2\rangle_4\Big), \\ CP_4|+\rangle|\psi_{\text{odd}}\rangle_4 =& \frac{1}{\sqrt{|c_1|^2+|c_3|^2}}\Big(c_1|+i\rangle|P_1\rangle_4 + c_3|-i\rangle|P_3\rangle_4\Big), \end{aligned} \tag{S72}$$

where $|\pm i\rangle = (|g\rangle \pm i|e\rangle)/\sqrt{2}$ are the σ_y eigenstates of the ancilla. If we are in the even subspace, we perform a projective measurement distinguishing between the remaining two states by measuring the ancilla along its x-axis, whereas if we are in the odd subspace we do so by measuring the ancilla along its y-axis. All together, this measurement will project the ququart onto one of the eigenstates $|P_n\rangle_4$ with probability $|c_n|^2$.

For $P_4 \in \{X_4, Z_4, \sqrt{\omega}X_4Z_4, X_4^2Z_4, \sqrt{\omega}X_4^3Z_4, X_4Z_4^2\}$, we compile the controlled Pauli gates CP_4 according to

$$\begin{aligned} CX_4 =& D(\sqrt{\pi/4}/2)\ \text{ECD}(\sqrt{\pi/4})\ \sigma_x, \\ CZ_4 =& D(i\sqrt{\pi/4}/2)\ \text{ECD}(i\sqrt{\pi/4})\ \sigma_x, \\ C(\sqrt{\omega}X_4Z_4) =& D(e^{i\pi/4}\sqrt{\pi/2}/2)\ \text{ECD}(e^{i\pi/4}\sqrt{\pi/2})\ \sigma_x, \\ CX_4^2Z_4 =& D((2+i)\sqrt{\pi/4}/2)\ \sigma_z(-\pi/2)\ \text{ECD}((2+i)\sqrt{\pi/4})\ \sigma_x, \\ C(\sqrt{\omega}X_4^3Z_4) =& D(e^{3\pi i/4}\sqrt{\pi/2}/2)\ \sigma_z(\pi/2)\ \text{ECD}(e^{3\pi i/4}\sqrt{\pi/2})\ \sigma_x, \\ CX_4Z_4^2 =& D((1+2i)\sqrt{\pi/4}/2)\ \sigma_z(-\pi/2)\ \text{ECD}((1+2i)\sqrt{\pi/4})\ \sigma_x, \end{aligned} \tag{S73}$$

as described in the Methods section of the main text. In our experiments we do not implement the unconditional displacements $D(\beta_{nm}/2)$ associated with each CP_4, but here they all commute through the entire circuit so their combined effect can be considered at the end of the two-part circuit. This means that our Pauli measurement sequence will apply an overall displacement $D(-\beta_{nm}/2)$ that brings us out of the code space (ignoring the additional effect of $D(-\beta_{nm})$ from the first part of the circuit, which applies an overall phase and keeps us in the code space). However, the envelope of our finite-energy code remains centered since our conditional displacements are symmetric about the origin.

To measure our GKP ququart in the parity basis $\{|s,n\rangle_4; s=\pm 1, n=0,1\}$, defined to be the simultaneous eigenstates of X_4^2 and Z_4^2 according to $X_4^2|s,n\rangle_4 = s|s,n\rangle_4$ and $Z_4^2|s,n\rangle_4 = (-1)^n|s,n\rangle_4$, we devised the circuit depicted in Fig. 3d of the main text. This circuit sequentially measures the eigenvalues of X_4^2 and Z_4^2 via two binary measurements of our ancilla. If the GKP ququart starts out in state $|\psi\rangle_4 = c_{+,0}|+,0\rangle_4 + c_{-,0}|-,0\rangle_4 + c_{+,1}|+,1\rangle_4 + c_{-,1}|-,1\rangle_4$ and the ancilla starts out in state $|+\rangle$, then the first part of the circuit entangles the two systems as

$$CX_4^2|+\rangle|\psi\rangle_4 = |+\rangle\Big(c_{+,0}|+,0\rangle_4 + c_{+,1}|+,1\rangle_4\Big) + |-\rangle\Big(c_{-,0}|-,0\rangle_4 + +c_{-,1}|-,1\rangle_4\Big), \tag{S74}$$

such that a subsequent measurement of the ancilla along its x axis constitutes a projective measurement on the ququart distinguishing between the ± 1 eigenspaces of X_4^2. Similarly, the second part of the circuit entangles the two systems as

$$CZ_4^2|+\rangle|\psi\rangle_4 = |+\rangle\Big(c_{+,0}|+,0\rangle_4 + c_{-,0}|-,0\rangle_4\Big) + |-\rangle\Big(c_{+,1}|+,1\rangle_4 + +c_{-,1}|-,1\rangle_4\Big), \tag{S75}$$

such that a subsequent measurement of the ancilla along its x axis constitutes a projective measurement on the ququart distinguishing between the ± 1 eigenspaces of Z_4^2. Note that when we compile CP_4^2 gates in terms of ECD gates, omitting the unconditional displacement means that we apply an additional P_4 operation, which keeps us in the code space. However, unlike our previous examples of Pauli measurements, in this case the X_4 operation applied by the first part of the parity measurement circuit does not commute through the second part of the circuit. This must be considered when decoding measurement results and determining the measurement backaction, but the analysis for taking this into account is straightforward.

To verify that our logical ququart Pauli and parity measurements work as intended, we prepare the maximally mixed state of the GKP ququart ρ_4^{mix} by performing 200 rounds of sBs starting from the cavity in vacuum, implement the two-part measurement circuit, and perform Wigner tomography of the cavity post-selected on the outcomes of the two binary measurements. The results of this experiment are shown in Fig. S 15, from which we can see that the measurements work as expected.

We simulate the fidelity of these logical measurements on the ququart by preparing Pauli eigenstate $|P_n\rangle_4$ or parity state $|\pm,m\rangle$ with finite-energy envelope size Δ, performing the corresponding logical measurement, and finding the

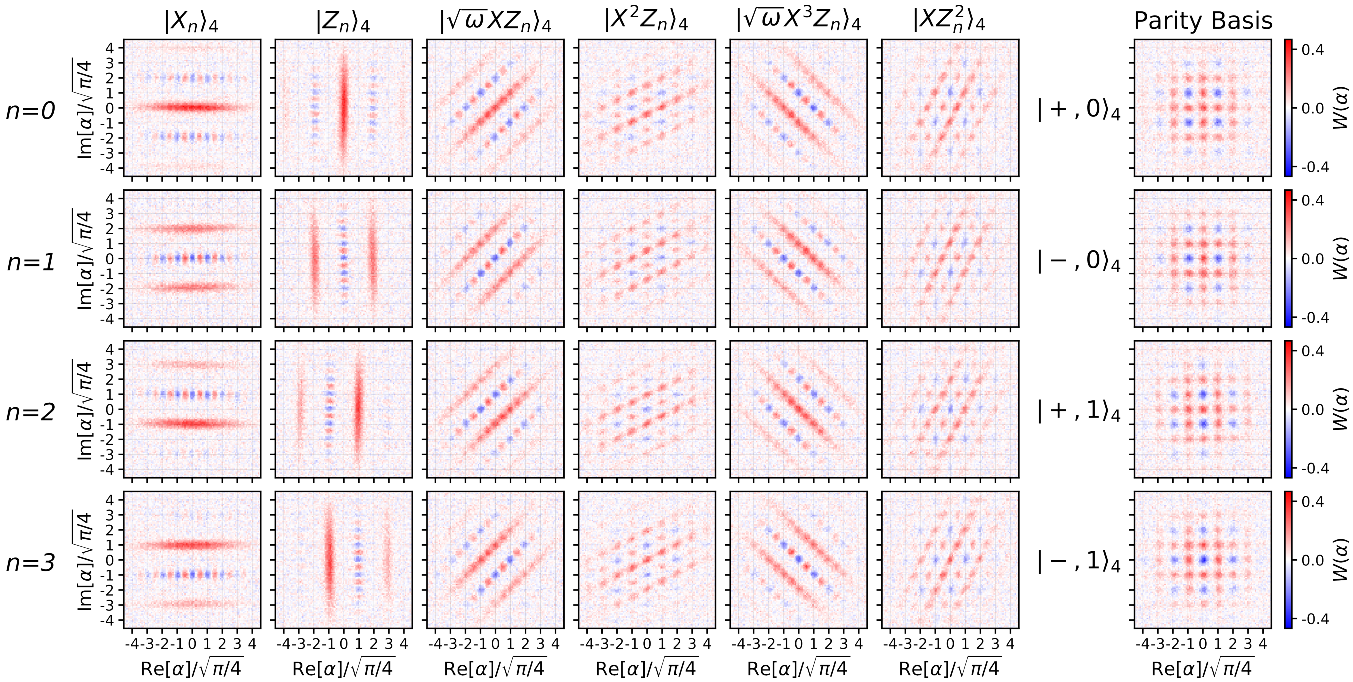

FIG. S 15. **GKP ququart Pauli and parity measurement backaction.** In each column, we implement a projective measurement with respect to the indicated basis and then perform Wigner tomography post-selected on the measurement outcomes.

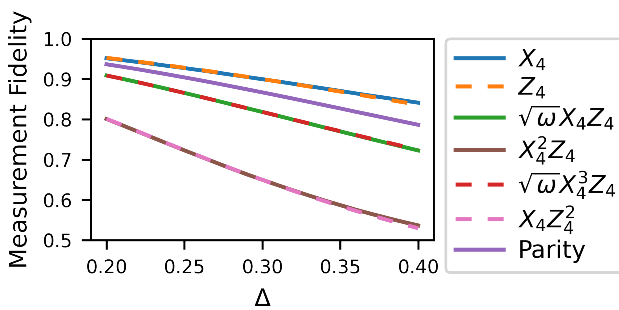

FIG. S 16. GKP ququart Pauli measurement fidelity (simulation)

probability $p(P_n|P_n)$ or $p(\pm, m|\pm, m)$ that we measure the state correctly at the end. We quantify the average measurement fidelity by

$$\begin{aligned}
\mathcal{F}_{P_4} &= \frac{1}{4}\Big[p(P_0|P_0) + p(P_1|P_1) + p(P_2|P_2) + +p(P_3|P_3)\Big], \\
\mathcal{F}_{\text{Parity}} &= \frac{1}{4}\Big[p(+,0|+,0) + p(-,0|-,0) + p(+,1|+,1) + p(-,1|-,1)\Big].
\end{aligned} \tag{S76}$$

The results of this simulation as a function of Δ are shown in Fig. S 16. As noted in the main text, these measurements are designed for the ideal code, leading to limited fidelity when applied to finite-energy codewords. We expect it is possible to adapt these measurements to the finite-energy case [19, 25, 27, 32], but we leave this for future work.

C. Optimized Ququart Beyond Break-even

We optimize the QEC protocol of the GKP ququart using a reinforcement learning (RL) agent [28] following the method described in Ref. [1] (also, see the Methods section of the main text). In Fig. S 17 we present both the reward signal and key parameters of the sBs circuit as a function of training epoch. For our interpretation of these results, see our discussion in Sec. IV C. The total duration of each sBs round is constrained to be 7 μs; the optimal

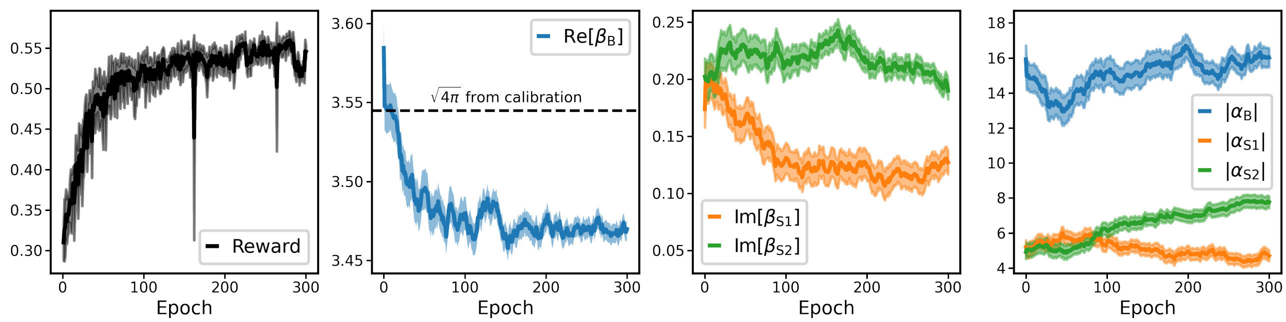

FIG. S 17. **GKP ququart RL training.** Lines indicate mean values while the shaded regions indicate the one-standard-deviation confidence interval.

protocol found by the RL training spends 3632 ns measuring and resetting the ancilla qubit, 1648 ns performing the sBs protocol, 1496 ns idling, and 224 ns executing FPGA sequencing instructions.

To evaluate the average channel fidelity of the optimal QEC protocol via Eq. (S58), we measure the probabilities $\langle P_n|\mathcal{E}^N_{\mathrm{opt}}(|P_n\rangle\langle P_n|)|P_n\rangle_4$ as a function of N for $n = 0, 1, 2, 3$ and $P \in \mathcal{P}_4 = \{X_4, Z_4, \sqrt{\omega}X_4Z_4, X_4^2Z_4, \sqrt{\omega}X_4^3Z_4, X_4Z_4^2\}$, and $\langle s, n|\mathcal{E}^N_{\mathrm{opt}}(|s, n\rangle\langle s, n|)|s, n\rangle_4$ as a function of N for $s = \pm1$ and $n = 0, 1$, where $\mathcal{E}^N_{\mathrm{opt}}$ is the channel corresponding to N rounds of the optimal QEC protocol. We measure these probabilities by preparing Pauli eigenstate $|P_n\rangle$ (or parity state $|s, n\rangle_4$), performing N rounds of QEC with the optimal protocol, and measuring the GKP ququart in the basis of Pauli operator P (or the ququart parity basis). The results of these twenty-eight experiments are presented in Fig. S 18. We then fit probabilities $\langle P_n|\mathcal{E}^N_{\mathrm{opt}}(|P_n\rangle\langle P_n|)|P_n\rangle_4$ and $\langle s, n|\mathcal{E}^N_{\mathrm{opt}}(|s, n\rangle\langle s, n|)|s, n\rangle_4$ to exponential decays and find the decay rates γ_{P_n} and $\gamma_{s,n}$. Note that we neglect the first two data points of these measurements, due to an artifact resulting from imperfect state preparation. These rates γ_{P_n} and $\gamma_{s,n}$ enable us to calculate the effective short-time depolarization rate of the optimized logical GKP ququart

$$\Gamma_4^{\mathrm{GKP}} = (620 \pm 2\ \mu\mathrm{s})^{-1}, \tag{S77}$$

using Eq. (S59). Comparing with $\Gamma_4^{\mathrm{Fock}} = (332 \pm 6\ \mu\mathrm{s})^{-1}$, we obtain a QEC gain of

$$G_4 = \Gamma_4^{\mathrm{Fock}}/\Gamma_4^{\mathrm{GKP}} = 1.87 \pm 0.03, \tag{S78}$$

well beyond the break-even point.

Lastly, we find the effective envelope size of our optimal GKP ququart by measuring its steady-state characteristic function $\mathcal{C}(\beta)$ near the origin of reciprocal phase space. In this experiment we run the optimal protocol for 300 rounds followed by characteristic function tomography, the result of which is shown in Fig. S 19. From this measurement we find an effective envelope size $\Delta_{\mathrm{eff}} = 0.246 \pm 0.001$, corresponding to average photon number $\langle a^\dagger a\rangle = (1/\Delta^2_{\mathrm{eff}} - 1)/2 = 7.76 \pm 0.07$. For more context on this analysis, see our discussion in Sec. IV C.

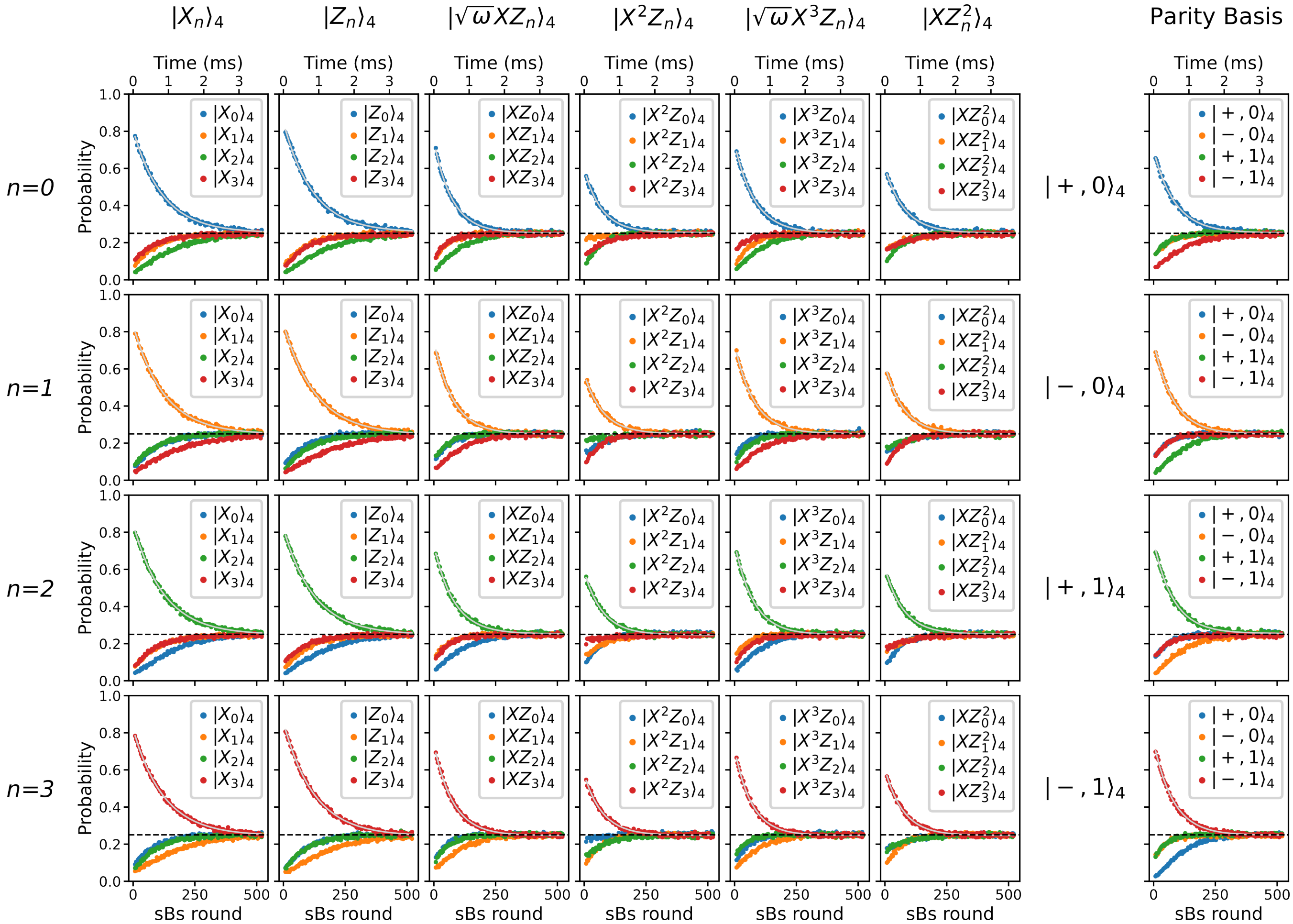

$\gamma_{P_n}^{-1}$ (μs)	$\lvert X_n\rangle_4$	$\lvert Z_n\rangle_4$	$\lvert\sqrt{\omega}XZ_n\rangle_4$	$\lvert X^2Z_n\rangle_4$	$\lvert\sqrt{\omega}X^3Z_n\rangle_4$	$\lvert XZ_n^2\rangle_4$
$n=0$	840 ± 8	836 ± 9	519 ± 6	507 ± 9	571 ± 7	562 ± 9
$n=1$	878 ± 10	918 ± 9	549 ± 7	536 ± 11	548 ± 7	528 ± 9
$n=2$	867 ± 10	867 ± 9	570 ± 7	520 ± 9	531 ± 7	525 ± 8
$n=3$	871 ± 9	872 ± 9	541 ± 6	529 ± 10	488 ± 6	521 ± 9

$\gamma_{\pm,m}^{-1}$ (μs)	
$\lvert+,0\rangle_4$	607 ± 8
$\lvert-,0\rangle_4$	565 ± 6
$\lvert+,1\rangle_4$	568 ± 7
$\lvert-,1\rangle_4$	559 ± 6

FIG. S 18. **Lifetime of the optimized GKP ququart.** The solid grey lines are fits to an exponential decay. The dashed black line indicates a probability of 1/4.

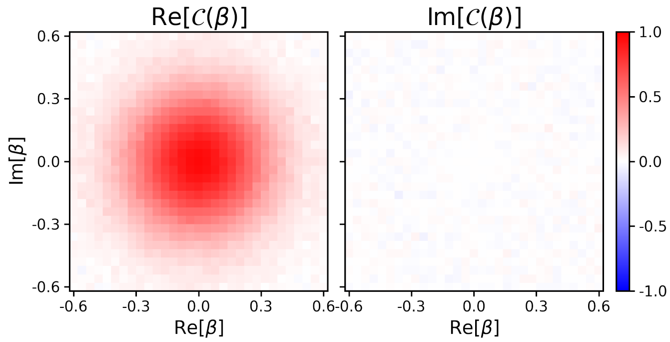

FIG. S 19. Steady-state characteristic function of the optimal GKP ququart QEC protocol, sampled near the origin of reciprocal phase space.

VII. SOURCES OF LOGICAL ERRORS

In this section we report the results of simulations aimed at estimating the relative contributions of different physical error sources to the effective decay rates Γ_d^{GKP} of our logical GKP qubit, qutrit, and ququart. We consider a simplified error model, consisting of transmon bit-flip errors during sBs at rate $\kappa_{1,q} = 1/T_{1,q}$ (i.e., combined heating and decay), transmon dephasing errors during sBs at rate $\kappa_{\phi,q} = 1/T_{2E,q} - 1/2T_{1,q}$, cavity photon loss during sBs at rate $\kappa_{1,c} = 1/T_{1,c}$, cavity photon loss during idling time at rate $\kappa_{1,c}$, and cavity dephasing during idling time at rate $\kappa_{\phi,c} = n_{\mathrm{th}}/T_{1,q}$. With this error model, we assume cavity dephasing primarily occurs during idling time, and can be fully attributed to thermal fluctuations of the transmon [5].

We simulate a simplified version of our optimal QEC protocols, where each ECD($\beta = |\beta|e^{i\theta_\beta}$) gate in sBs is realized by evolving under the Hamiltonian

$$H_{CD} = \frac{i}{2}\chi\alpha\left(e^{i\theta_\beta}a^\dagger - e^{-i\theta_\beta}a\right)\sigma_z, \tag{S79}$$

for time $t = |\beta|/\chi\alpha$ followed by an ancilla σ_x gate, rather than performing a pulse-level simulation of the compiled ECD gate. For each ECD gate in sBs we use the $\alpha_{S1,B,S2}$ found by the reinforcement learning agent, and use $\beta_{S1,B,S2}$ scaled by a factor of $\sqrt{\pi d}/|\beta_B|$, since we assume the deviation we find between $\sqrt{\pi d}$ and β_B is due to miscalibration. During idling time, we evolve under the identity.

To isolate the relative contributions of each type of physical error, we simulate our optimal QEC protocols in the presence of each individual source of error on its own. As a basis of comparison, we then simulate in the presence of all errors. Finally, to estimate the extent to which different errors compound with one another, we simulate in the presence of all errors occurring during sBs, and in the presence of all errors occurring during idling. We perform all of our simulations using a combination of Dynamiqs [33] and QuTiP [34]. The results of our simulations for the optimal GKP qubit are presented in Table S VI, those for the optimal GKP qutrit are presented in Table S VII, and those for the optimal GKP ququart are presented in Table S VIII. Note that we calculate the relative contribution of each error type (expressed as a percentage) by comparing ${\Gamma_d^{\mathrm{GKP}}}^{-1}$ of that error type to the case of all errors. We emphasize that with all of the simplifications and assumptions made in performing this simulation, these results are not meant to be directly compared with our experimental measurements. Rather, they should be viewed heuristically, providing a basis for analyzing the limiting factors of our QEC protocol and how they change with qudit dimension d.

We find that the most significant sources of logical errors are transmon bit-flips during sBs, cavity photon loss during idling, and cavity dephasing during idling. The rate of logical errors caused by transmon bit-flips remains fairly constant as we increase d from 2 to 4, limiting the lifetime to about 6.5 ms in $d = 2$ and $d = 3$, and to about 6 ms in $d = 4$. However, since the overall lifetime ${\Gamma_d^{\mathrm{GKP}}}^{-1}$ decreases as we increase d, the relative contribution of transmon bit-flips to the total logical error rate decreases. On the other hand, the rate of logical errors caused by cavity photon loss during idling increases as we go from $d = 2$ to 4, as does the relative contribution of these errors to the total logical error rate. As we argue in the main text, this is due to having a smaller Δ as we increase d, which means our codewords have more energy and lose photons more quickly as a result. We find that cavity dephasing during idling is the dominant source of error for $d = 2, 3$ and 4, and its relative contribution increases as we increase d. For $d = 4$, it is responsible for about half of the logical error rate. As discussed in the main text, we attribute this to the larger lattice spacing of GKP qudits, which means the codewords contain information further out in phase space, making them more susceptible to cavity dephasing errors.

We find that all of these errors compound with one another, leading to larger logical error rates when combined than on their own, as was previously found in the error budget simulations of Ref. [16]. Interestingly, this is also true for all errors during sBs and all errors during idling; when these error rates are added, they only account for about 90% of the total logical error rate in $d = 2, 3$, and 4 obtained when both are combined in the same simulation.

Error Type	Γ_X^{-1} (ms)	Γ_Z^{-1} (ms)	Γ_{XZ}^{-1} (ms)	$\Gamma_2^{\mathrm{GKP}^{-1}}$ (ms)	%
Transmon $\kappa_{1,q}$ during sBs	8.69	8.69	4.35	6.52	25
Transmon $\kappa_{\phi,q}$ during sBs	3230	3000	1550	2330	0.07
Cavity $\kappa_{1,c}$ during sBs	1210	1890	720	1100	0.15
All errors during sBs	8.60	8.60	4.31	6.46	25
Cavity $\kappa_{1,c}$ during idling	50.3	50.3	25.2	37.8	4.3
Cavity $\kappa_{\phi,c}$ during idling	6.74	6.74	3.41	5.08	32
All errors during idling	3.40	3.40	1.72	2.56	63
All errors	2.15	2.15	1.09	1.62	100

Table S VI. Error budgeting of the optimal GKP qubit. For each Pauli basis P_2, we only simulate the $|P_0\rangle_2$ state.

Error Type	Γ_X^{-1} (ms)	Γ_Z^{-1} (ms)	Γ_{XZ}^{-1} (ms)	$\Gamma_{X^2Z}^{-1}$ (ms)	$\Gamma_3^{\mathrm{GKP}^{-1}}$ (ms)	%
Transmon $\kappa_{1,q}$ during sBs	9.73	9.67	4.87	4.86	6.48	11
Transmon $\kappa_{\phi,q}$ during sBs	860	1180	660	620	780	0.09
Cavity $\kappa_{1,c}$ during sBs	370	340	180	160	230	0.3
All errors during sBs	9.42	9.41	4.73	4.74	6.3	12
Cavity $\kappa_{1,c}$ during idling	13.8	13.8	6.91	6.91	9.2	7.9
Cavity $\kappa_{\phi,c}$ during idling	2.42	2.42	1.22	1.22	1.62	45
All errors during idling	1.40	1.40	0.71	0.71	0.94	78
All errors	1.08	1.08	0.55	0.55	0.73	100

Table S VII. Error budgeting of the optimal GKP qutrit. For each Pauli basis P_3, we only simulate the $|P_0\rangle_3$ state.

Error Type	Γ_X^{-1} (ms)	Γ_Z^{-1} (ms)	Γ_{XZ}^{-1} (ms)	$\Gamma_{X^2Z}^{-1}$ (ms)	$\Gamma_{X^3Z}^{-1}$ (ms)	$\Gamma_{XZ^2}^{-1}$ (ms)	$\Gamma_{+,0}^{-1}$ (ms)	$\Gamma_4^{\mathrm{GKP}^{-1}}$ (ms)	%
Transmon $\kappa_{1,q}$ during sBs	9.63	9.64	4.85	5.64	4.85	5.64	7.38	5.96	7.6
Transmon $\kappa_{\phi,q}$ during sBs	590	580	270	250	260	260	300	320	0.14
Cavity $\kappa_{1,c}$ during sBs	190	190	98	95	97	92	100	120	0.38
All errors during sBs	9.22	9.21	4.66	5.37	4.66	5.37	6.93	5.72	7.9
Cavity $\kappa_{1,c}$ during idling	6.35	6.35	3.25	3.05	3.24	3.06	3.24	3.91	12
Cavity $\kappa_{\phi,c}$ during idling	1.42	1.41	0.75	0.67	0.75	0.67	0.73	0.88	51
All errors during idling	0.87	0.87	0.47	0.40	0.47	0.40	0.45	0.54	83
All errors	0.73	0.73	0.39	0.34	0.39	0.34	0.39	0.45	100

Table S VIII. Error budgeting of the optimal GKP ququart. For each Pauli basis P_4, we only simulate the $|P_0\rangle_4$ state.

[1] V. V. Sivak, A. Eickbusch, B. Royer, S. Singh, I. Tsioutsios, S. Ganjam, A. Miano, B. L. Brock, A. Z. Ding, L. Frunzio, S. M. Girvin, R. J. Schoelkopf, and M. H. Devoret, Nature **616**, 50 (2023).
[2] A. P. M. Place, L. V. H. Rodgers, P. Mundada, B. M. Smitham, M. Fitzpatrick, Z. Leng, A. Premkumar, J. Bryon, A. Vrajitoarea, S. Sussman, G. Cheng, T. Madhavan, H. K. Babla, X. H. Le, Y. Gang, B. Jäck, A. Gyenis, N. Yao, R. J. Cava, N. P. De Leon, and A. A. Houck, Nature Communications **12**, 1779 (2021).
[3] C. Wang, X. Li, H. Xu, Z. Li, J. Wang, Z. Yang, Z. Mi, X. Liang, T. Su, C. Yang, G. Wang, W. Wang, Y. Li, M. Chen, C. Li, K. Linghu, J. Han, Y. Zhang, Y. Feng, Y. Song, T. Ma, J. Zhang, R. Wang, P. Zhao, W. Liu, G. Xue, Y. Jin, and H. Yu, npj Quantum Information **8**, 3 (2022).
[4] S. Ganjam, Y. Wang, Y. Lu, A. Banerjee, C. U. Lei, L. Krayzman, K. Kisslinger, C. Zhou, R. Li, Y. Jia, M. Liu, L. Frunzio, and R. J. Schoelkopf, Nature Communications **15**, 3687 (2024).
[5] M. Reagor, W. Pfaff, C. Axline, R. W. Heeres, N. Ofek, K. Sliwa, E. Holland, C. Wang, J. Blumoff, K. Chou, M. J. Hatridge, L. Frunzio, M. H. Devoret, L. Jiang, and R. J. Schoelkopf, Physical Review B **94**, 014506 (2016).
[6] C. Axline, M. Reagor, R. Heeres, P. Reinhold, C. Wang, K. Shain, W. Pfaff, Y. Chu, L. Frunzio, and R. J. Schoelkopf, Applied Physics Letters **109**, 042601 (2016).
[7] A. A. Clerk and D. W. Utami, Physical Review A **75**, 042302 (2007).
[8] Z. Wang, S. Shankar, Z. Minev, P. Campagne-Ibarcq, A. Narla, and M. Devoret, Physical Review Applied **11**, 014031 (2019).
[9] S. Rosenblum, P. Reinhold, M. Mirrahimi, L. Jiang, L. Frunzio, and R. J. Schoelkopf, Science **361**, 266 (2018).
[10] A. Koottandavida, I. Tsioutsios, A. Kargioti, C. R. Smith, V. R. Joshi, W. Dai, J. D. Teoh, J. C. Curtis, L. Frunzio, R. J. Schoelkopf, and M. H. Devoret, Physical Review Letters **132**, 180601 (2024).
[11] A. Z. Ding, B. L. Brock, A. Eickbusch, A. Koottandavida, N. E. Frattini, R. G. Cortinas, V. R. Joshi, S. J. de Graaf, B. J. Chapman, S. Ganjam, L. Frunzio, R. J. Schoelkopf, and M. H. Devoret, "Quantum control of an oscillator with a Kerr-cat qubit," (2024), arXiv:2407.10940 [quant-ph].
[12] A. Eickbusch, V. Sivak, A. Z. Ding, S. S. Elder, S. R. Jha, J. Venkatraman, B. Royer, S. M. Girvin, R. J. Schoelkopf, and M. H. Devoret, Nature Physics **18**, 1464 (2022).
[13] A. Eickbusch, "ECD Control," Github Repository, https://github.com/alec-eickbusch/ECD_control.
[14] B. Vlastakis, G. Kirchmair, Z. Leghtas, S. E. Nigg, L. Frunzio, S. M. Girvin, M. Mirrahimi, M. H. Devoret, and R. J. Schoelkopf, Science **342**, 607 (2013).
[15] C. Flühmann and J. Home, Physical Review Letters **125**, 043602 (2020).
[16] P. Campagne-Ibarcq, A. Eickbusch, S. Touzard, E. Zalys-Geller, N. E. Frattini, V. V. Sivak, P. Reinhold, S. Puri, S. Shankar, R. J. Schoelkopf, L. Frunzio, M. Mirrahimi, and M. H. Devoret, Nature **584**, 368 (2020).
[17] D. Gottesman, A. Kitaev, and J. Preskill, Physical Review A **64**, 012310 (2001).
[18] A. L. Grimsmo and S. Puri, PRX Quantum **2**, 020101 (2021).
[19] B. Royer, S. Singh, and S. Girvin, Physical Review Letters **125**, 260509 (2020).
[20] J. Zak, Physical Review Letters **19**, 1385 (1967).
[21] A. Kenfack and K. Życzkowski, Journal of Optics B: Quantum and Semiclassical Optics **6**, 396 (2004).
[22] M. A. Nielsen, Physics Letters A **303**, 249 (2002).
[23] W. K. Wootters and B. D. Fields, Annals of Physics **191**, 363 (1989).
[24] C. Flühmann, T. L. Nguyen, M. Marinelli, V. Negnevitsky, K. Mehta, and J. P. Home, Nature **566**, 513 (2019).
[25] B. De Neeve, T.-L. Nguyen, T. Behrle, and J. P. Home, Nature Physics **18**, 296 (2022).
[26] B. M. Terhal and D. Weigand, Physical Review A **93**, 012315 (2016).
[27] J. Hastrup, K. Park, J. B. Brask, R. Filip, and U. L. Andersen, npj Quantum Information **7**, 17 (2021).
[28] V. Sivak, A. Eickbusch, H. Liu, B. Royer, I. Tsioutsios, and M. Devoret, Physical Review X **12**, 011059 (2022).
[29] Z. Chen, J. Kelly, C. Quintana, R. Barends, B. Campbell, Y. Chen, B. Chiaro, A. Dunsworth, A. Fowler, E. Lucero, E. Jeffrey, A. Megrant, J. Mutus, M. Neeley, C. Neill, P. O'Malley, P. Roushan, D. Sank, A. Vainsencher, J. Wenner, T. White, A. Korotkov, and J. M. Martinis, Physical Review Letters **116**, 020501 (2016).
[30] Y. Shalibo, Y. Rofe, D. Shwa, F. Zeides, M. Neeley, J. M. Martinis, and N. Katz, Physical Review Letters **105**, 177001 (2010).
[31] G. J. Grabovskij, T. Peichl, J. Lisenfeld, G. Weiss, and A. V. Ustinov, Science **338**, 232 (2012).
[32] I. Rojkov, P. M. Röggla, M. Wagener, M. Fontboté-Schmidt, S. Welte, J. Home, and F. Reiter, Physical Review Letters **133**, 100601 (2024).
[33] P. Guilmin, R. Gautier, A. Bocquet, and É. Genois, "Dynamiqs: an open-source python library for gpu-accelerated and differentiable simulation of quantum systems," (2024), Github Repository, https://github.com/dynamiqs/dynamiqs.
[34] J. Johansson, P. Nation, and F. Nori, Computer Physics Communications **183**, 1760 (2012).